Computers and Mathematics with Applications 147 (2023) 164–184

Contents lists available at ScienceDirect

Computers and Mathematics with Applications

journal homepage: www.elsevier.com/locate/camwa

IgA-BEM for 3D Helmholtz problems using conforming and non-conforming multi-patch discretizations and B-spline tailored numerical integration

Bruno Degli Esposti [a,b], Antonella Falini [c], Tadej Kanduč [d,e,*], Maria Lucia Sampoli [f], Alessandra Sestini [a]

[a] Department of Mathematics and Computer Science, University of Florence, Viale Morgagni 67, Firenze, Italy
[b] Department of Mathematics, University of Giessen, Arndtstrasse 2, Giessen, Germany
[c] Department of Informatics, University of Bari Aldo Moro, Via Orabona 4, Bari, Italy
[d] Faculty of Mathematics and Physics, University of Ljubljana, Jadranska ulica 19, 1000 Ljubljana, Slovenia
[e] Faculty of Mechanical Engineering, University of Ljubljana, Aškerčeva cesta 6, 1000 Ljubljana, Slovenia
[f] Department of Information Engineering and Mathematics, University of Siena, Via Roma 56, Siena, Italy

ARTICLE INFO

Keywords:
Helmholtz equation
Isogeometric Analysis (IgA)
Boundary Element Method (BEM)
Non-conforming discretization
Singular and nearly singular integral
Numerical integration
B-spline quasi-interpolation

ABSTRACT

An Isogeometric Boundary Element Method (IgA-BEM) is considered for the numerical solution of Helmholtz problems on 3D bounded or unbounded domains, admitting a smooth multi-patch representation of their finite boundary surface. The discretization spaces are formed by C^0 inter-patch continuous functional spaces whose restriction to a patch simplifies to the span of tensor product B-splines composed with the given patch NURBS parameterization. Both conforming and non-conforming spaces are allowed, so that local refinement is possible at the patch level. For regular and singular integration, the proposed model utilizes a numerical procedure defined on the support of each trial B-spline function, which makes possible a function-by-function implementation of the matrix assembly phase. Spline quasi-interpolation is the common ingredient of all the considered quadrature rules; in the singular case it is combined with a B-spline recursion over the spline degree and with a singularity extraction technique, extended to the multi-patch setting for the first time. A threshold selection strategy is proposed to automatically distinguish between nearly singular and regular integrals. The non-conforming C^0 joints between spline spaces on different patches are implemented as linear constraints based on knot removal conditions, and do not require a hierarchical master-slave relation between neighbouring patches. Numerical examples on relevant benchmarks show that the expected convergence orders are achieved with uniform discretization and a small number of uniformly spaced quadrature nodes.

1. Introduction

Isogeometric Analysis (IgA) [1] is a powerful tool to obtain a numerical solution of problems governed by partial differential equations, introduced in the literature at the beginning of the new millennium. This new paradigm was motivated by the observation that in engineering applications a domain is described by its boundary parametric representation generated by Computer Aided Design (CAD) software. For this aim CAD relies on flexible forms, often based on multi-patch tensor product B-spline or rational B-spline (NURBS) spaces, suited also for applications [2]. The IgA idea consists in adopting the CAD functional spaces also for approximating the solution of the differential problem, taking into account the well-known optimal approximation power of spline spaces [3,4]. The increasing success of the IgA paradigm in the context of both domain and boundary element methods is easily explained considering that, besides being capable to keep an exact representation of complex domains described in a multi-patch CAD form, IgA formulations guarantee a certain level of accuracy with considerably less degrees of freedom than traditional Finite Element Analysis (FEA), which relies on larger piecewise polynomial spaces with lower inter-element smoothness within each patch [5]. The attractiveness of IgA is even higher for Boundary Element Methods (BEMs), see for example [6–11] and references therein, because, in contrast to domain methods like Finite Element Methods (FEM), they do not require any preliminary volumetric parameterization, which can be a remarkably time consuming task. BEMs rely on a boundary integral formulation of

* Corresponding author at: Faculty of Mathematics and Physics, University of Ljubljana, Jadranska ulica 19, 1000 Ljubljana, Slovenia.
E-mail address: tadej.kanduc@fmf.uni-lj.si (T. Kanduč).

https://doi.org/10.1016/j.camwa.2023.07.012
Received 22 October 2022; Received in revised form 13 June 2023; Accepted 15 July 2023

the problem, which can be derived whenever the fundamental solution of the associated differential operator is known. Hence, they require only the definition of a mesh on the boundary of the domain, which is a much easier task especially in the IgA context, where the CAD representation of the boundary is available.

The precursor of this work, dealing with 3D IgA-BEM, is presented in [12], where exterior Laplace problems with Dirichlet boundary conditions on single patch domains are considered and, in order to deal also with screen problems, an indirect boundary integral formulation is adopted. In this paper the IgA multi-patch formulation of BEMs (multi-patch IgA-BEMs) is considered by the authors for the first time. The discretization splines spaces are generalized to non-conforming C^0 setting, which allow adaptivity at the patch level. Such approach is based on a direct boundary integral formulation of problems governed by the Helmholtz equation in 3D bounded or unbounded domains, equipped with either Dirichlet or Neumann boundary conditions. Such problems are of interest in acoustics to model radiation and rigid scattering in the frequency domain [13], where radiation refers to the pressure field produced by an object vibrating within a fluid (usually air or water), while rigid scattering relates to the disturbance caused by an obstacle immersed within an existing acoustic field. The adopted Boundary Integral Equation (BIE) discretized with a collocation approach is the so-called conventional BIE (CBIE), which involves only weakly singular integrals and is augmented with the Sommerfeld radiation condition at infinity for exterior problems. The Helmholtz operator can thus be simply written as a sum of the Laplacian Δ with an identity operator scaled with a positive parameter κ^2. However, even when dealing with exterior Helmholtz problems admitting a unique solution, such BIE generates spurious solutions when κ^2 is an eigenvalue of $-\Delta$ for the considered boundary conditions. This is the reason why other papers also relying on IgA-BEMs for the numerical solution of the Helmholtz equation introduce its alternative Burton-Miller (BM) boundary integral formulation, which does not suffer from such a drawback. Obtained as a linear combination of the mentioned CBIE with the hypersingular BIE (HBIE) also paired with the Helmholtz operator, the BM integral formulation is clearly more difficult, see for example [14], where it is combined with a regularization technique to avoid to deal with hypersingular integrals in the assembly phase. However, successive researches have given numerical evidence that, when κ^2 is not an eigenvalue of $-\Delta$, better numerical results are achieved by using the simpler CBIE, see for example [15,16]. Since clearly only a finite number of different values of the parameter κ^2 can be considered and this can be anyway sufficient for a reasonable reconstruction of an associated time-dependent acoustic field, in this work the IgA-BEM approach was applied just to the CBIE associated with Helmholtz, with the implicit assumption to avoid values of κ^2 equal to eigenvalues of $-\Delta$.

The IgA-BEM implementation in this study relies on the B-spline tailored cubature formulas for regular and weakly singular integrals, introduced in [17] in the setting of weakly singular surface integrals. The theoretical convergence order of such rules is analyzed in this work for the first time. Since the proposed quadrature schemes are constructed on the support of every bivariate B-spline, a function-by-function implementation of the matrix assembly phase can be adopted, similarly to work for 2D Laplace problems in [18]. This attractive feature markedly reduces the amount of data access during the assembly phase, compared to a more common element-by-element strategy. Another remarkable feature of the proposed quadratures is the freedom of choice for the quadrature nodes – no reparameterization of nodes near the singularities is needed and, by choosing uniformly spaced nodes in the parametric space for all the required regular and singular numerical integrations, it ensures the possibility of using a small overall number of unique nodes. By applying a singularity subtraction technique on singular integrals, the singular and regular part of the integrand are effectively separated. Thanks to the thorough study developed in [19] for the weakly singular kernel expansions, the continuity of the regularized integrands can be controlled and the developed integration rules have consequently better approximation properties for general smooth geometry parameterizations. A novelty in this work is a careful decoupling of integrals appearing in the Helmholtz BIE into simpler, real and imaginary, regular and singular integrals. An original strategy for the automatic detection of near singularity is also introduced. Another new key feature lies in coupling the integration routines with multi-patch geometry representations; when the source point and the integration domain are separated by a patch interface, the unmatching parameterization across it poses an additional challenge. To overcome difficulties of this type, a novel approximate singularity subtraction technique is introduced and analyzed for nearly singular inter-patch integrals. It replaces the source point with its projection on an extrapolation of the patch surface, where the integration has to be performed.

The paper is organized as follows. The next section introduces the Helmholtz problem and its conventional boundary integral formulation for both Dirichlet and Neumann boundary conditions. Then, in Section 3 the multi-patch IgA setting for the standard CAD representation of a bounded or unbounded domain is described, as well as the finite dimensional functional spaces adopted for the analysis. Section 4 describes the developed quadrature formulas, based on the tensor-product formulation of a discrete spline quasi-interpolation approach. The formulas are combined with a subtraction regularization technique and applied to the single and double layer Helmholtz kernels. In Section 5 the results obtained for several benchmark problems are reported and commented, relying on both the conforming and non-conforming discretization approaches and including a preliminary experiment on a non-smooth geometry. Finally some conclusive remarks are given in Section 6. Appendix A reports a theoretical analysis on the nature of the considered singular kernels on smooth geometries. Appendix B reports a proof for non-conforming discretization spaces that the system matrix is a square matrix. The matrix is nonsingular if all of its collocation conditions are replaced by corresponding point-wise interpolation conditions (the importance of these properties is explained in Section 3.3, see Remark 1).

2. The Helmholtz problem and its boundary integral formulation

3D potential problems described by the Helmholtz equation with Dirichlet or Neumann boundary conditions are studied on domains $\Omega \subset \mathbb{R}^3$ admitting a connected and compact boundary surface $\Gamma = \partial\Omega$,

$$\begin{cases} \Delta u + \kappa^2 u = 0 & \text{in } \Omega, \\ u = u_{\mathrm{D}} \quad \text{or} \quad \frac{\partial u}{\partial \mathbf{n}} = u_{\mathrm{N}} & \text{on } \Gamma, \end{cases} \tag{1}$$

where $u : \Omega \to \mathbb{C}$ denotes the unknown *potential*, $\mathbf{n}$ the unit normal on Γ pointing outward from Ω and $\kappa > 0$. When the domain is a finite volume, the problem is *interior* and the notation $\Omega^{[i]}$ is used to underline the type of this domain, when it is useful. In the opposite case, the set $\Omega^{[e]}$ is used for an *exterior* problem. Concerning the regularity of the boundary surface Γ, it is assumed to be smooth, at least without self-intersections and with a tangent plane well defined at each point and varying continuously. Note that for exterior problems, equation (1) has to be augmented with an additional condition, the so-called *Sommerfeld radiation condition*,

$$\frac{\partial u}{\partial r} - i\kappa u = o\left(\frac{1}{r}\right), \tag{2}$$

where r denotes the point distance from the origin of the reference system and i is the imaginary unit; see for example [13]. This condition at infinity is necessary to ensure for any positive κ the existence and uniqueness of the solution u for exterior Helmholtz problems for both Dirichlet and Neumann boundary conditions. Uniqueness of u for interior problems is ensured when κ^2 is not an eigenvalue of the reversed Laplacian operator $-\Delta$ in Ω.[1] Regarding the regularity of the

[1] The scalar λ is an eigenvalue for $-\Delta$ if there exists a non-vanishing function u_λ such that $-\Delta u_\lambda = \lambda u_\lambda$, also fulfilling homogeneous boundary condition of the

weak solution u of (1), observe that u belongs to the Sobolev space $H^1(\Omega)$, provided that, for Dirichlet (Neumann) boundary conditions, $u_D \in H^{1/2}(\Gamma)$, $\left(u_N \in H^{-1/2}(\Gamma)\right)$.

The Helmholtz equation is of particular interest in acoustic because the solution $u = u(\mathbf{x}, \kappa)$, $\mathbf{x} \in \Omega$ of (1) can be interpreted as the inverse Fourier transform [21] of the time-dependent scattered pressure field $p = p(\mathbf{x}, t)$ generated by the scatterer in a given fluid domain, which fulfills the wave equation,

$$\frac{1}{c_f^2}\,\frac{\partial^2 p}{\partial t^2} = \Delta p. \tag{3}$$

Indeed, by defining $\check{p}$ as the inverse Fourier transform of p with respect to t

$$\check{p} = \check{p}(\mathbf{x}, \nu) := \frac{1}{2\pi}\int_{-\infty}^{+\infty} p(\mathbf{x}, t) e^{i\nu t}\, dt$$

it follows that $\check{p}$ satisfies the Helmholtz equation with $\kappa = \nu/c_f$ and that the solution p to the wave equation can be recovered as the Fourier transform of $\check{p}$ with respect to ν:

$$p = \int_{-\infty}^{+\infty} \check{p}(\mathbf{x}, \nu) e^{-i\nu t}\, d\nu\,.$$

This is of interest because focusing on a single angular frequency ν at a time lets us effectively remove the time dependence from the wave equation and hence deal with a differential problem formulated exclusively in terms of spatial variables.

In order to approximate the solution of (1) with IgA-BEMs, the Conventional Boundary Integral Equation (CBIE) associated to the Helmholtz equation is considered and derived by the direct approach,

$$\int_\Gamma \mathcal{G}_\kappa(\mathbf{x}, \mathbf{y}) \frac{\partial u}{\partial \mathbf{n}}(\mathbf{y}) d\Gamma_\mathbf{y} = c(\mathbf{x}) u(\mathbf{x}) + \int_\Gamma \frac{\partial \mathcal{G}_\kappa}{\partial \mathbf{n}_\mathbf{y}}(\mathbf{x}, \mathbf{y})\, u(\mathbf{y})\, d\Gamma_\mathbf{y}, \qquad \mathbf{x} \in \Gamma, \tag{4}$$

where $r := \|\mathbf{r}\|_2$ with $\mathbf{r} := \mathbf{x} - \mathbf{y}$. The kernel $\mathcal{G}_\kappa$ and its derivative with respect to the exterior unit normal $\mathbf{n}$ to Γ computed in the point $\mathbf{y} \in \Gamma$ are defined as

$$\mathcal{G}_\kappa(\mathbf{x}, \mathbf{y}) := \frac{1}{4\pi r} e^{\mathrm{i}\kappa r}, \qquad \frac{\partial \mathcal{G}_\kappa}{\partial \mathbf{n}_\mathbf{y}}(\mathbf{x}, \mathbf{y}) = \frac{1}{4\pi r} e^{\mathrm{i}\kappa r}\left(-\frac{1}{r} + \mathrm{i}\kappa\right) \frac{\partial r}{\partial \mathbf{n}_\mathbf{y}},$$

with

$$\frac{\partial r}{\partial \mathbf{n}_\mathbf{y}} = -\frac{\mathbf{r} \cdot \mathbf{n}_\mathbf{y}}{r}, \qquad c(\mathbf{x}) := -\int_\Gamma \frac{\partial \mathcal{G}_0}{\partial \mathbf{n}_\mathbf{y}}(\mathbf{x}, \mathbf{y}) d\Gamma_\mathbf{y}\,, \tag{5}$$

being $c(\mathbf{x}) \equiv 1/2$ for the assumed smooth surface Γ. The restrictions of u and $(\partial u/\partial \mathbf{n})(\mathbf{y})$ to Γ (in the sense of traces) are usually called *Cauchy data*. One of them corresponds to the available boundary datum, and the other to the unknown. By separating the real and imaginary parts of $\mathcal{G}_\kappa$, the kernel is rewritten as

$$\mathcal{G}_\kappa = \frac{1}{4\pi}\left(\frac{\cos(\kappa r)}{r} + \mathrm{i}\frac{\sin(\kappa r)}{r}\right). \tag{6}$$

Note that the real part of $\mathcal{G}_\kappa$ goes to infinity as $1/r$ when $r \to 0^+$, while its imaginary part tends to $\kappa/(4\pi)$. The other kernel involved in (4) is $\partial \mathcal{G}_\kappa/\partial \mathbf{n}_\mathbf{y}$, which can be rewritten as follows, again separating its real and imaginary parts,

$$\frac{\partial \mathcal{G}_\kappa}{\partial \mathbf{n}_\mathbf{y}}(\mathbf{x}, \mathbf{y}) = \frac{1}{4\pi}\left[\left(\frac{\mathbf{r} \cdot \mathbf{n}_\mathbf{y}}{r^3}\left(\cos(\kappa r) + \kappa r \sin(\kappa r)\right)\right) + \mathrm{i}\frac{\mathbf{r} \cdot \mathbf{n}_\mathbf{y}}{r^2}\left(\frac{\sin(\kappa r)}{r} - \kappa\cos(\kappa r)\right)\right]. \tag{7}$$

assigned type. It is possible to prove that the operator $-\Delta$ admits only positive eigenvalues, which define an unbounded infinite sequence of positive numbers depending on the considered kind of boundary conditions and on the shape of the finite domain Ω, see for example [20].

For a regular surface Γ described by a regular smooth parameterization, the quantity $\mathbf{r} \cdot \mathbf{n}_\mathbf{y}/r^2$ is bounded for $r \to 0^+$, but in general it is not continuous at $r = 0$; see Appendix A for a proof. The bounded behaviour at $r = 0$ of such quantity implies that, analogously to $\mathcal{G}_\kappa$, the kernel $\partial \mathcal{G}_\kappa/\partial \mathbf{n}_\mathbf{y}$ is just weakly singular, see Section 9.1 in [22] and also the analytical related insights explicitly reported in Appendix A. Indeed, its real part goes to infinity as $1/r$ when $r \to 0^+$ while its imaginary part tends to zero because $\mathbf{r} \cdot \mathbf{n}_\mathbf{y}/r^2$ remains bounded and it is multiplied by a factor going to zero.

Clearly, when the boundary conditions in (1) are of Dirichlet type, the unknown in (4) is the flux $\phi := (\partial u/\partial \mathbf{n})|\Gamma$, belonging to $H^{-1/2}(\Gamma)$, and the CBIE becomes

$$\int_\Gamma \mathcal{G}_\kappa(\mathbf{x}, \mathbf{y}) \phi(\mathbf{y}) d\Gamma_\mathbf{y} = c(\mathbf{x}) u_D(\mathbf{x}) + \int_\Gamma \frac{\partial \mathcal{G}_\kappa}{\partial \mathbf{n}_\mathbf{y}}(\mathbf{x}, \mathbf{y}) u_D(\mathbf{y}) d\Gamma_\mathbf{y}, \qquad \mathbf{x} \in \Gamma. \tag{8}$$

Note that this is an integral equation of the general type

$$V_\kappa \phi(\mathbf{x}) = f(\mathbf{x}), \qquad \mathbf{x} \in \Gamma, \tag{9}$$

where f denotes a known function and the single layer operator $V_\kappa : H^{-1/2}(\Gamma) \to H^{1/2}(\Gamma)$ is an elliptic isomorphism defined as

$$V_\kappa \phi(\mathbf{x}) := \int_\Gamma \mathcal{G}_\kappa(\mathbf{x}, \mathbf{y}) \phi(\mathbf{y})\, d\Gamma_\mathbf{y}.$$

Conversely, when Neumann conditions are dealt with, the unknown in (4) is the acoustic potential $\phi := u|\Gamma$, with $\phi \in H^{1/2}(\Gamma)$, and the CBIE becomes

$$\int_\Gamma \frac{\partial \mathcal{G}_\kappa}{\partial \mathbf{n}_\mathbf{y}}(\mathbf{x}, \mathbf{y}) \phi(\mathbf{y})\, d\Gamma_\mathbf{y} + c(\mathbf{x}) \phi(\mathbf{x}) = \int_\Gamma \mathcal{G}_\kappa(\mathbf{x}, \mathbf{y}) u_N(\mathbf{y}) d\Gamma_\mathbf{y} \qquad \mathbf{x} \in \Gamma. \tag{10}$$

This is an integral equation of the general type

$$(c(x) I + K_\kappa)\phi(\mathbf{x}) = f(\mathbf{x}), \qquad \mathbf{x} \in \Gamma, \tag{11}$$

associated to the operator $cI + K_\kappa$, where I denotes the identity operator and $K_\kappa : H^{1/2}(\Gamma) \to H^{1/2}(\Gamma)$ is the following double layer operator,

$$K_\kappa \phi(\mathbf{x}) := \int_\Gamma \frac{\partial \mathcal{G}_\kappa}{\partial \mathbf{n}_\mathbf{y}}(\mathbf{x}, \mathbf{y})\, \phi(\mathbf{y})\, d\Gamma_\mathbf{y}.$$

Note that the right-hand side f in both (9) and (11) is equal to the right-hand side of (8) and (10), respectively.

If ϕ is available, the solution $u = u(\mathbf{x}, \kappa)$, $\mathbf{x} \in \Omega$, of the boundary value problem in (1) is given by the so-called *representation formula*,

$$u(\mathbf{x}, \kappa) = \pm\left(\int_\Gamma \mathcal{G}_\kappa(\mathbf{x}, \mathbf{y})\, \frac{\partial u}{\partial \mathbf{n}}(\mathbf{y})\, d\Gamma_\mathbf{y} - \int_\Gamma \frac{\partial \mathcal{G}_\kappa}{\partial \mathbf{n}_\mathbf{y}}(\mathbf{x}, \mathbf{y})\, u(\mathbf{y})\, d\Gamma_\mathbf{y}\right), \qquad \mathbf{x} \in \Omega, \tag{12}$$

where the sign is positive if $\Omega = \Omega^{[i]}$ (interior problem) and negative otherwise. Note that the numerical implementation of this formula is not completely trivial because, when $\mathbf{x}$ is very close to Γ, nearly singular integrals have to be approximated. However, one can be merely interested in ϕ or in evaluating u just at points sufficiently far from Γ. For example, when an exterior problem is taken into account, often the interest is just in the *far field pattern* of u, that is into the recovery of u_∞, where

$$u_\infty(\mathbf{w}) := \lim_{r \to \infty} r e^{-i\kappa r} u(r\mathbf{w}), \qquad \mathbf{w} \in S^2,$$

where S^2 is a unit sphere in $\mathbb{R}^3$ centred at the origin of the considered reference system. In such case the following formula that only requires rules for regular integrals is convenient [15],

$$u_\infty(\mathbf{w}) = \frac{1}{4\pi}\int_\Gamma \left(i\kappa u(\mathbf{y})(\mathbf{w} \cdot \mathbf{n}(\mathbf{y})) + \frac{\partial u}{\partial \mathbf{n}}(\mathbf{y})\right) e^{-i\kappa(\mathbf{w} \cdot \mathbf{y})} d\Gamma_\mathbf{y}.$$

3. Multi-patch isogeometric model

In this section the IgA-BEM model is introduced with respect to the geometry representation and the discretization space to express the numerical solution. The flexibility to model complex geometries in the 3D case is facilitated by adopting its multi-patch formulation. Let us assume that the boundary Γ is a union of M patches $\Gamma^{(\ell)}, \ell = 1, \dots, M$, and for $k \neq \ell$ it holds $\Gamma^{(k)} \cap \Gamma^{(\ell)} = \emptyset$ and $\partial\Gamma^{(k)} \cap \partial\Gamma^{(\ell)}$ is a boundary edge curve of each patch, a corner point of each patch or an empty set. To each patch $\Gamma^{(\ell)}$ a geometry map $\mathbf{F}^{(\ell)}$ is assigned, such that $\overline{\Gamma^{(\ell)}} = \text{Image}(\mathbf{F}^{(\ell)})$, $\mathbf{F}^{(\ell)} : [0,1]^2 \to \overline{\Gamma^{(\ell)}} \subset \mathbb{R}^3$ is regular and belongs to $C^2([0,1]^2)$. Each $\mathbf{F}^{(\ell)}$ is written in the following standard NURBS form [2],

$$\mathbf{F}^{(\ell)}(\mathbf{t}) := \frac{\sum_{\mathbf{i} \in \mathcal{J}^{\mathbf{T}_{\mathrm{g}}^{(\ell)}}} w_{\mathbf{i}}^{(\ell)} \mathbf{Q}_{\mathbf{i}}^{(\ell)} \hat{B}_{\mathbf{i},\mathbf{d}_{\mathrm{g}}}^{\mathbf{T}_{\mathrm{g}}^{(\ell)}}(\mathbf{t})}{\sum_{\mathbf{i} \in \mathcal{J}^{\mathbf{T}_{\mathrm{g}}^{(\ell)}}} w_{\mathbf{i}}^{(\ell)} \hat{B}_{\mathbf{i},\mathbf{d}_{\mathrm{g}}}^{\mathbf{T}_{\mathrm{g}}^{(\ell)}}(\mathbf{t})}, \quad \mathbf{t} \in [0,1]^2, \tag{13}$$

The bidimensional knot array $\mathbf{T}_{\mathrm{g}}^{(\ell)}$ associated with the ℓ-th patch, $\mathbf{T}_{\mathrm{g}}^{(\ell)} := T_{\mathrm{g},1}^{(\ell)} \times T_{\mathrm{g},2}^{(\ell)}$ ($T_{\mathrm{g},1}^{(\ell)}$ and $T_{\mathrm{g},2}^{(\ell)}$ are open knot vectors with entries in the interval $[0,1]$) together with multi-index set $\mathcal{J}^{\mathbf{T}_{\mathrm{g}}^{(\ell)}}$ define the bi-degree $\mathbf{d}_{\mathrm{g}} = (d_{\mathrm{g},1}, d_{\mathrm{g},2})$ tensor product B-spline basis $\hat{B}_{\mathbf{i},\mathbf{d}_{\mathrm{g}}}^{\mathbf{T}_{\mathrm{g}}^{(\ell)}}(\mathbf{t}) := \hat{B}_{i_1,d_{\mathrm{g},1}}^{T_{\mathrm{g},1}^{(\ell)}}(t_1)\, \hat{B}_{i_2,d_{\mathrm{g},2}}^{T_{\mathrm{g},2}^{(\ell)}}(t_2)$ defined on $[0,1]^2$ in variable $\mathbf{t} := (t_1, t_2)$ and $\mathbf{i} := (i_1, i_2) \in \mathcal{J}^{\mathbf{T}_{\mathrm{g}}^{(\ell)}}$. A set $\{\mathbf{Q}_{\mathbf{i}}^{(\ell)} \in \mathbb{R}^3 : \mathbf{i} \in \mathcal{J}^{\mathbf{T}_{\mathrm{g}}^{(\ell)}}\}$ defines a net of control points which, together with the associated set of positive weights $\{w_{\mathbf{i}}^{(\ell)} \in \mathbb{R} : \mathbf{i} \in \mathcal{J}^{\mathbf{T}_{\mathrm{g}}^{(\ell)}}\}$, is the basic element typically used in the CAD environment to design free-form surfaces. For the sake of lighter notation, the superscript for knot arrays (e.g. $\mathbf{T}_{\mathrm{g}}^{(\ell)}$) is omitted, whenever a distinction between different knot arrays is not necessary. When two patches share an edge $C_{k,\ell} := \partial\Gamma^{(k)} \cap \partial\Gamma^{(\ell)}$ for $k \neq \ell$, the shared edge is a NURBS curve. In the following, this curve is assumed to be parameterized with the same geometry map for both patches, up to reversion in directions and direction swapping in the parametric space.

As commonly assumed in a more generalized IgA-BEM setting, the unknown Cauchy datum ϕ is approximated in a functional space, whose restriction to $\overline{\Gamma^{(\ell)}}$ is composed of a B-spline space defined in $[0,1]^2$ and the inverse of the geometric mapping $\mathbf{F}^{(\ell)}$ (the space shares the same approximation power with the related NURBS counterpart). All the B-splines appearing in the geometry description of equation (13) can be exactly represented in the discretization space. Therefore, the bi-degree $\mathbf{d}$ for the discretization space is greater or equal to $\mathbf{d}_{\mathrm{g}}$ and all the knots of $T_{\mathrm{g},i}^{(\ell)}$ are included in the corresponding ℓ-th discretization knot vector with multiplicity increased at least by $d_i - d_{\mathrm{g},i}, i = 1, 2$.

The method presented in this paper can handle also a more decoupled relation between the geometric and the discretization knot arrays, and the corresponding spline degrees – this setting is additionally motivated in order to compare the method with the results of some numerical experiments developed in other papers. Hence, in the rest of the article it is assumed that the discretization space has its own degree $\mathbf{d} = (d_1, d_2)$ (common to all patches) and open knot vectors, $T_j^{(\ell)}$, $j = 1, 2$. By denoting with $h_j^{(\ell)}$ the maximal distance between successive knots in $T_j^{(\ell)}$, setting $h^{(\ell)} := \max\{h_1^{(\ell)}, h_2^{(\ell)}\}$, introducing the bi-dimensional knot array $\mathbf{T}^{(\ell)} := T_1^{(\ell)} \times T_2^{(\ell)}$ and set of bivariate indices $\mathcal{J}^{\mathbf{T}^{(\ell)}}$ for the basis functions, let $\hat{\mathcal{S}}_{h^{(\ell)}}^{(\ell)}$ denote the spline space generated by the tensor product B-spline basis $\{\hat{B}_{\mathbf{j},\mathbf{d}}^{\mathbf{T}^{(\ell)}} : \mathbf{j} = (j_1, j_2) \in \mathcal{J}^{\mathbf{T}^{(\ell)}}\}$ of bi-degree $\mathbf{d}$, defined on $[0,1]^2$.

3.1. Inter-patch discontinuous spaces

When no continuity constraint is imposed across patches for the basis functions, the global space used to approximate the unknown Cauchy datum ϕ is

$$S_{h,\mathbf{d}} := \text{span}\{B_{\mathbf{j},\mathbf{d}}^{\mathbf{T}^{(\ell)}} : \mathbf{j} \in \mathcal{J}^{\mathbf{T}^{(\ell)}}, \quad \ell = 1, \dots, M\},$$

where $h := \max\{h^{(\ell)}, \ell = 1, \dots, M\}$ and

$$B_{\mathbf{j},\mathbf{d}}^{\mathbf{T}^{(\ell)}}(\mathbf{x}) = \begin{cases} \hat{B}_{\mathbf{j},\mathbf{d}}^{\mathbf{T}^{(\ell)}} \circ \mathbf{F}^{(\ell)^{-1}}(\mathbf{x}), & \text{if } \mathbf{x} \in \Gamma^{(\ell)}, \\ 0, & \text{otherwise.} \end{cases}$$

Clearly with this setting the global number N_{DOF} of degrees of freedom used to approximate ϕ is

$$N_{\mathrm{DOF}} = \sum_{\ell=1}^{M} |\mathcal{J}^{\mathbf{T}^{(\ell)}}|,$$

where $|\mathcal{J}^{\mathbf{T}^{(\ell)}}|$ is the cardinality of the set. In this setting it is convenient to select $|\mathcal{J}^{\mathbf{T}^{(\ell)}}|$ distinct collocation points belonging to the interior of each patch $\Gamma^{(\ell)}$, $\ell = 1, \dots, M$. In particular, let $\mathbf{x}_{\mathbf{j}}^{(\ell)} = \mathbf{F}^{(\ell)}(\mathbf{s}_{\mathbf{j}})$, $\mathbf{j} \in \mathcal{J}^{\mathbf{T}^{(\ell)}}$, where $\{\mathbf{s}_{\mathbf{j}}^{(\ell)} : \mathbf{j} \in \mathcal{J}^{\mathbf{T}^{(\ell)}}\}$ denotes a set of points in $(0,1)^2$, defined as the Cartesian product of two sets of abscissas, the so-called improved Greville abscissas associated to $T_1^{(\ell)}$ and $T_2^{(\ell)}$ [23]. Recall that the improved Greville abscissae related to a set of Greville abscissae $\bar{\xi}_1, \bar{\xi}_2, \dots, \bar{\xi}_n$, are Greville abscissae whose first and last elements are modified as follows:

$$\tilde{\xi}_1 = \bar{\xi}_1 + \omega(\bar{\xi}_2 - \bar{\xi}_1), \quad \tilde{\xi}_n = \bar{\xi}_n - \omega(\bar{\xi}_n - \bar{\xi}_{n-1}), \quad \text{with } 0 < \omega < 1. \tag{14}$$

Thus, a discrete version of the integral formulation of the Dirichlet (8) or Neumann (10) problem is obtained by approximating ϕ in the finite dimensional composite space $S_{h,\mathbf{d}}$. The applied collocation method leads to a linear system

$$A\,\boldsymbol{\alpha} = \boldsymbol{\beta}. \tag{15}$$

The unknown entries in the vector $\boldsymbol{\alpha}$ are the coefficients which allow to define the approximation ϕ_h of ϕ in the space $S_{h,\mathbf{d}}$ patch-wisely as follows,

$$\phi_h(\mathbf{x}) := \sum_{\ell=1}^{M} \sum_{\mathbf{j} \in \mathcal{J}^{(\ell)}} \alpha_{\mathbf{j}}^{(\ell)} B_{\mathbf{j},\mathbf{d}}^{\mathbf{T}^{(\ell)}}(\mathbf{x}), \qquad \mathbf{x} \in \Gamma.$$

The square system matrix $A \in \mathbb{C}^{N_{\mathrm{DOF}} \times N_{\mathrm{DOF}}}$ and the right-hand side vector $\boldsymbol{\beta} \in \mathbb{C}^{N_{\mathrm{DOF}}}$ have a block representation, $A = (A^{(k,\ell)})$, $\boldsymbol{\beta} = (\boldsymbol{\beta}^{(k)})$, for $k, \ell = 1, \dots, M$, where $A^{(k,\ell)} \in \mathbb{C}^{|\mathcal{J}_k| \times |\mathcal{J}_\ell|}$ and $\boldsymbol{\beta}^{(k)} \in \mathbb{C}^{|\mathcal{J}_k|}$. For each pair of patches $\Gamma^{(k)}, \Gamma^{(\ell)}$, the rows (columns) of the related submatrix are ordered by using a lexicographical ordering of the elements in $\mathcal{J}^{\mathbf{T}^{(k)}}$ ($\mathcal{J}^{\mathbf{T}^{(\ell)}}$), namely identifying a single index i with $\mathbf{i}$ and j with $\mathbf{j}$. After this simplification, for the Dirichlet case such entries read as follows in both the physical and the parametric domain,

$$A_{i,j}^{(k,\ell)} := \int_{\Gamma^{(\ell)}} \mathcal{G}_\kappa(\mathbf{x}_{\mathbf{i}}^{(k)}, \mathbf{y}) B_{\mathbf{j},\mathbf{d}}^{\mathbf{T}^{(\ell)}}(\mathbf{y})\, d\Gamma = \int_{[0,1]^2} \mathcal{G}_\kappa(\mathbf{x}_{\mathbf{i}}^{(k)}, \mathbf{F}^{(\ell)}(\mathbf{t})) \hat{B}_{\mathbf{j},\mathbf{d}}^{\mathbf{T}^{(\ell)}}(\mathbf{t})\, J^{(\ell)}(\mathbf{t})\, d\mathbf{t}, \tag{16}$$

$$\begin{aligned} \beta_i^{(k)} &:= \sum_{\ell=1}^{M} \int_{\Gamma^{(\ell)}} \frac{\partial \mathcal{G}_\kappa}{\partial \mathbf{n}_{\mathbf{y}}}(\mathbf{x}_{\mathbf{i}}^{(k)}, \mathbf{y})\, u_{\mathrm{D}}(\mathbf{y})\, d\Gamma + \frac{1}{2} u_{\mathrm{D}}(\mathbf{x}_{\mathbf{i}}^{(k)}) \\ &= \sum_{\ell=1}^{M} \int_{[0,1]^2} \frac{\partial \mathcal{G}_\kappa}{\partial \mathbf{n}_{\mathbf{y}}}(\mathbf{x}_{\mathbf{i}}^{(k)}, \mathbf{F}^{(\ell)}(\mathbf{t}))\, u_{\mathrm{D}}(\mathbf{F}^{(\ell)}(\mathbf{t}))\, J^{(\ell)}(\mathbf{t})\, d\mathbf{t} + \frac{1}{2} u_{\mathrm{D}}(\mathbf{x}_{\mathbf{i}}^{(k)}), \end{aligned} \tag{17}$$

where $i = 1, \dots, |\mathcal{J}^{(k)}|$, $j = 1, \dots, |\mathcal{J}^{(\ell)}|$ and $J^{(\ell)}$ represents the infinitesimal surface area element on the ℓ-th patch,

$$J^{(\ell)}(\cdot) := \left\| \frac{\partial \mathbf{F}^{(\ell)}}{\partial t_1}(\cdot) \times \frac{\partial \mathbf{F}^{(\ell)}}{\partial t_2}(\cdot) \right\|_2.$$

Conversely, for the Neumann case the matrix entries are

$$A_{i,j}^{(k,\ell)} := \int_{\Gamma^{(\ell)}} \frac{\partial \mathcal{G}_\kappa}{\partial \mathbf{n}_\mathbf{y}}(\mathbf{x}_\mathbf{i}^{(k)}, \mathbf{y}) B_{\mathbf{j},\mathbf{d}}^{\mathbf{T}^{(\ell)}}(\mathbf{y})\, d\Gamma + \frac{1}{2} B_{\mathbf{j},\mathbf{d}}^{\mathbf{T}^{(\ell)}}(\mathbf{x}_\mathbf{i}^{(k)})$$
$$= \int_{[0,1]^2} \frac{\partial \mathcal{G}_\kappa}{\partial \mathbf{n}_\mathbf{y}}(\mathbf{x}_\mathbf{i}^{(k)}, \mathbf{F}^{(\ell)}(\mathbf{t})) \hat{B}_{\mathbf{j},\mathbf{d}}^{\mathbf{T}^{(\ell)}}(\mathbf{t}) J^{(\ell)}(\mathbf{t})\, d\mathbf{t} + \frac{1}{2} \hat{B}_{\mathbf{j},\mathbf{d}}^{\mathbf{T}^{(\ell)}}(\mathbf{x}_\mathbf{i}^{(k)}), \tag{18}$$

$$\beta_i^{(k)} := \sum_{\ell=1}^{M} \int_{\Gamma^{(\ell)}} \mathcal{G}_\kappa(\mathbf{x}_\mathbf{i}^{(k)}, \mathbf{y})\, u_\mathrm{N}(\mathbf{y})\, d\Gamma$$
$$= \sum_{\ell=1}^{M} \int_{[0,1]^2} \mathcal{G}_\kappa(\mathbf{x}_\mathbf{i}^{(k)}, \mathbf{F}^{(\ell)}(\mathbf{t}))\, u_\mathrm{N}(\mathbf{F}^{(\ell)}(\mathbf{t}))\, J^{(\ell)}(\mathbf{t})\, d\mathbf{t}, \tag{19}$$

Referring for brevity just to the Dirichlet case, an equivalent scaled expression of these entries is reported below, since it will be useful in Section 4 to develop a reasonably scaled procedure to detect nearly singular integrals to be computed during the assembly phase. Denoting with μ_ℓ a reference length for the ℓ-th patch (e.g., the square root of its area or its diameter), with φ_ℓ the associated uniform scaling such that $\tilde{\mathbf{z}} = \varphi_\ell(\mathbf{z}) = \mathbf{z}/\mu_\ell$ and with $\tilde{\Gamma}^{(\ell)}$ the conformally scaled version of the ℓ-th patch, the matrix entries are equal to

$$A_{i,j}^{(k,\ell)} = \mu_\ell \int_{\tilde{\Gamma}^{(\ell)}} \mathcal{G}_{\kappa_\ell}(\varphi_\ell(\mathbf{x}_\mathbf{i}^{(k)}), \tilde{\mathbf{y}}) B_{\mathbf{j},\mathbf{d}}^{\mathbf{T}^{(\ell)}}(\mu_\ell \tilde{\mathbf{y}})\, d\tilde{\Gamma}$$
$$= \mu_\ell \int_{[0,1]^2} \mathcal{G}_{\kappa_\ell}(\varphi_\ell(\mathbf{x}_\mathbf{i}^{(k)}), \tilde{\mathbf{F}}^{(\ell)}(\mathbf{t})) \hat{B}_{\mathbf{j},\mathbf{d}}^{\mathbf{T}^{(\ell)}}(\mathbf{t})\, \tilde{J}^{(\ell)}(\mathbf{t})\, d\mathbf{t}, \tag{20}$$

$$\beta_i^{(k)} = \sum_{\ell=1}^{M} \int_{\tilde{\Gamma}^{(\ell)}} \frac{\partial \mathcal{G}_{\kappa^{(\ell)}}}{\partial \mathbf{n}_{\tilde{\mathbf{y}}}}(\varphi_\ell(\mathbf{x}_\mathbf{i}^{(k)}), \tilde{\mathbf{y}})\, u_\mathrm{D}(\mu_\ell \tilde{\mathbf{y}})\, d\tilde{\Gamma} + \frac{1}{2} u_\mathrm{D}(\mathbf{x}_\mathbf{i}^{(k)})$$
$$= \sum_{\ell=1}^{M} \int_{[0,1]^2} \frac{\partial \mathcal{G}_{\kappa_\ell}}{\partial \mathbf{n}_{\tilde{\mathbf{y}}}}(\varphi_\ell(\mathbf{x}_\mathbf{i}^{(k)}), \tilde{\mathbf{F}}^{(\ell)}(\mathbf{t}))\, u_\mathrm{D}(\mu_\ell \tilde{\mathbf{F}}^{(\ell)}(\mathbf{t}))\, \tilde{J}^{(\ell)}(\mathbf{t})\, d\mathbf{t}$$
$$+ \frac{1}{2} u_\mathrm{D}(\mathbf{x}_\mathbf{i}^{(k)}), \tag{21}$$

where $\tilde{\mathbf{F}}^{(\ell)} := \mathbf{F}^{(\ell)}/\mu_\ell$, $\tilde{J}^{(\ell)}$ is the related infinitesimal scaled area element and $\kappa_\ell := \kappa \mu_\ell$.

3.2. Inter-patch conforming continuous spaces

Let us denote the space of B-spline functions that join with C^0 regularity across patches by $S_{h,\mathbf{d}}^0 := S_{h,\mathbf{d}} \cap C^0(\Gamma)$. For the time being, let us assume that any two adjacent patches $\Gamma^{(k)}, \Gamma^{(\ell)}$ with a common boundary curve $C_{k,\ell}$ have the same knot vector on the edges of the patches. Namely, on the k-th patch the knot vector $T_1^{(k)}$ is considered if $\mathbf{F}^{(k)}(t_1, 0)$ or $\mathbf{F}^{(k)}(t_1, 1)$ define the curve $C_{k,\ell}$, and in the other case it is $T_2^{(k)}$ that is considered. The same procedure is done for ℓ-th patch. The assumption then states that the two vectors $T_i^{(k)}$, $T_j^{(\ell)}$ need to coincide (up to a possible reversion of one knot sequence, e.g., when $\mathbf{F}^{(k)}(1, t_2) = \mathbf{F}^{(\ell)}(1, 1 - t_2)$). If this is the case, the two knot vectors are said to be *conforming*, and the same adjective will also be used to describe discretization spaces on neighbouring patches that coincide when restricted to the common edge.

The so-called interior basis functions for $S_{h,\mathbf{d}}^0$ include all basis functions $B_{\mathbf{j},\mathbf{d}}^{\mathbf{T}^{(k)}}$ from $S_{h,\mathbf{d}}$ whose corresponding B-splines $\hat{B}_{\mathbf{j},\mathbf{d}}^{\mathbf{T}^{(k)}}$ vanish on $\partial([0,1]^2)$. The so-called edge or vertex basis functions are obtained by identifying and summing together the remaining basis functions from $S_{h,\mathbf{d}}$ with shared knot vectors. More precisely, each edge basis function in $S_{h,\mathbf{d}}^0$ specifically associated to $C_{k,\ell}$ is a sum of two remaining (not interior) functions $B_{\mathbf{i},\mathbf{d}}^{\mathbf{T}^{(k)}}$ and $B_{\mathbf{j},\mathbf{d}}^{\mathbf{T}^{(\ell)}}$ from $S_{h,\mathbf{d}}$, that vanish at the endpoints of $C_{k,\ell}$ and satisfy $\hat{B}_{\mathbf{i},\mathbf{d}}^{\mathbf{T}^{(k)}} \circ \mathbf{F}^{(k)^{-1}}(\mathbf{x}) = \hat{B}_{\mathbf{j},\mathbf{d}}^{\mathbf{T}^{(\ell)}} \circ \mathbf{F}^{(\ell)^{-1}}(\mathbf{x})$ for every $\mathbf{x} \in C_{k,\ell}$. Similarly, a vertex function associated to a patch corner vertex $\mathbf{x}_v$ is defined as a sum of all basis functions $B_{\mathbf{i},\mathbf{d}}^{\mathbf{T}^{(k)}}$ from $S_{h,\mathbf{d}}$, $k = 1, \dots, M$ and $\mathbf{i} \in \mathcal{J}^{\mathbf{T}^{(k)}}$ that satisfy $\hat{B}_{\mathbf{i},\mathbf{d}}^{\mathbf{T}^{(k)}} \circ \mathbf{F}^{(k)^{-1}}(\mathbf{x}_v) \neq 0$.

In all experiments with the C^0 continuous basis the collocation points are fixed as a set of images of Cartesian products of standard Greville abscissas on $[0,1]^2$, mapped to $\overline{\Gamma^{(k)}}$ via map $\mathbf{F}^{(k)}$ for all $k = 1, \dots, M$, and by counting just once the repeated points which appear on the boundary curves of patches.

The approximate solution ϕ_h is constructed similarly to the discontinuous case, bearing in mind a variation in the collocation points and a sum of adequate entries in (16), (18) over all suitable ℓ to evaluate integrals that span over the patches $\Gamma^{(\ell)}$ adjacent to $\Gamma^{(k)}$.

3.3. Inter-patch non-conforming continuous spaces

The assumption of conformity greatly simplifies the implementation of globally continuous discretization spaces, but also severely limits the possibility of adapting $h^{(\ell)}$ on every patch to better approximate local features of the unknown Cauchy datum ϕ. This is because the constraint $T_i^{(k)} = T_j^{(\ell)}$ for all edges $C_{k,\ell}$ (up to reversion of some knot vectors) propagates globally across patches, so that the refinement of the discretization space on a single patch usually ends up causing most other spaces to be unnecessarily refined. It is for this reason that *non-conforming* spaces have been introduced in the literature; the first work in this sense is [24].

So far, only the hierarchically non-conforming case has been considered, see for example [1,25]. Two knot vectors are said to be *hierarchically* non-conforming if either $T_i^{(k)} \subseteq T_j^{(\ell)}$ or $T_i^{(k)} \supseteq T_j^{(\ell)}$ holds for all edges $C_{k,\ell}$. This assumption is in general a good compromise between ease of implementation and computational efficiency. Nevertheless, the inclusion constraint still propagates globally across patches, and in practice this means that, without a dyadic uniform subdivision of knot vectors (or similar nesting strategies), unrelated and non-local knots may be forcibly included into knot vectors of a patch. However, limiting knot vectors to dyadic uniform subdivisions clearly hinders the flexibility of the non-conforming approach, and potentially introduces inefficiencies due to excessive refinement.

In this work, the implementation of non-conforming C^0 joints between B-spline spaces on neighbouring patches is done in full generality, that is, without assuming any relation between $T_i^{(k)}$ and $T_j^{(\ell)}$, i.e., no hierarchical master-slave relation between neighbouring patches is required. This means that, in theory, knot vectors $T_1^{(k)}$ and $T_2^{(k)}$ can be chosen independently on each patch $\Gamma^{(k)}$, based only on information local to $\Gamma^{(k)}$. In practice, however, some kind of compatibility assumption is still needed on the knot vectors $T_i^{(k)}$ and $T_j^{(\ell)}$ on the two sides of each edge for the global spline space $S_{h,\mathbf{d}}^0$ to have full approximation power as $h \to 0$. To see why, let $S(T, d)$ be the univariate spline space defined by the open knot vector T and the polynomial degree d. Then, for every pair of knot vectors T, T' with a common parametric domain $[0,1]$, it holds that

$$S(T \cap T', d) = S(T, d) \cap S(T', d), \tag{22}$$

assuming that the intersection operation between knot vectors takes knot multiplicities into account (i.e., the minimum multiplicity of each node is kept in the intersection). On the one hand, identity (22) ensures that a C^0 connection between neighbouring patches is always possible, because the space Π_d of polynomials on $[0,1]$ of degree at most d is included in the intersection $S(T_i^{(k)}, d) \cap S(T_j^{(\ell)}, d)$. On the other hand, if $T_i^{(k)}$ and $T_j^{(\ell)}$ share no internal knots, then the intersection $S(T_i^{(k)}, d) \cap S(T_j^{(\ell)}, d)$ is merely equal to Π_d, whose dimension as a vector space is independent of h. This implies that the approximation power of $S_{h,\mathbf{d}}^0$ in a neighbourhood of size h of edge $C_{k,\ell}$ is severely limited and, as a consequence, its global order of approximation is at most $h^{1/2}$ in the $L^2(\Gamma)$ norm, which is far from the optimal order h^{d+1}. A necessary condition to avoid this issue is to satisfy

$$\liminf_{h\to 0} \frac{\left|T_i^{(k)}(h) \cap T_j^{(\ell)}(h)\right|}{\left|T_i^{(k)}(h)\right|} > 0 \quad \text{and} \quad \liminf_{h\to 0} \frac{\left|T_i^{(k)}(h) \cap T_j^{(\ell)}(h)\right|}{\left|T_j^{(\ell)}(h)\right|} > 0 \tag{23}$$

for a given knot vector refinement strategy $T_i^{(k)}(h), T_j^{(\ell)}(h)$. This new constraint (23) is not hard to enforce in practice, and does not propagate globally across patches. Even in the special case of uniform subdivisions of knot vectors, it makes it possible to take intermediate refinement steps between consecutive powers of two by, e.g., allowing numbers of the form $3 \cdot 2^n$.

From an implementation point of view, elimination of redundant degrees of freedom as in the conforming C^0 case is no longer an attractive option. The reason is that a basis for $S^0_{h,\mathbf{d}}$ would no longer have a tensor-product structure on each patch, so it is better in practice to work with the discontinuous basis of Section 3.1 and enforce the continuity constraints across each edge $\mathcal{C}_{k,\ell}$ by including suitable equations in the final linear system $A\boldsymbol{\alpha} = \boldsymbol{\beta}$. Naturally, for A to be a square matrix, the number of collocation conditions must be reduced accordingly.

Inspired by conditions coming from spline interpolation problems, let $\hat{G}(T, d)$ be the vector of standard Greville abscissas defined by the knot vector T and the polynomial degree d, and let $G_{k,\ell}(T, d)$ be its pushforward to the edge $\mathcal{C}_{k,\ell}$. Then the global list of collocation points is built as follows: start from all the vertices of every patch (with no duplicates), then for each edge $\mathcal{C}_{k,\ell}$ add the elements $G_{k,\ell}(T_i^{(k)} \cap T_j^{(\ell)}, d)$ (except for the endpoints, because they are already included as patch vertices), and finally for each patch $\Gamma^{(k)}$ include the standard bivariate Greville points that do not belong to $\partial\Gamma^{(k)}$. Collocation of the conventional boundary integral equations (8) or (10) at the points on this list leads to a linear system

$$A_{\text{coll}}\, \boldsymbol{\alpha} = \boldsymbol{\beta}_{\text{coll}}, \tag{24}$$

with $\dim(S^0_{h,\mathbf{d}})$ rows and $\dim(S_{h,\mathbf{d}})$ columns.

As for the continuity constraints, there are two conceptually distinct but algebraically equivalent ways to obtain them. The first is a generalization to the non-hierarchical non-conforming setting of the coupling equations based on virtual knot insertion introduced in [24]. For any given edge $\mathcal{C}_{k,\ell}$, let $\boldsymbol{\alpha}_{k,\ell}$ be the subvector of $\boldsymbol{\alpha}$ that contains all the elements of the form $\alpha_{\mathbf{j}}^{(k)}$ such that $B_{\mathbf{j},\mathbf{d}}^{\mathbf{T}^{(k)}}$ does not vanish on $\mathcal{C}_{k,\ell}$. Moreover, let $\mathbf{T}_{k,\ell}$ be the knot insertion matrix from the basis of B-splines on the space $S(T_i^{(k)}, d)$ to the basis of B-splines on the space $S(T_i^{(k)} \cup T_j^{(\ell)}, d)$, where the union operation between knot vectors is defined so as to take knot multiplicities into account.

Then, assuming that the elements of $\boldsymbol{\alpha}_{k,\ell}$ and $\boldsymbol{\alpha}_{\ell,k}$ are suitably ordered along edge $\mathcal{C}_{k,\ell}$, the non-conforming continuity constraint across the edge simply reads

$$\mathbf{T}_{k,\ell}\, \boldsymbol{\alpha}_{k,\ell} - \mathbf{T}_{\ell,k}\, \boldsymbol{\alpha}_{\ell,k} = 0. \tag{25}$$

Unfortunately, it is not enough to iterate over all edges and grow the linear system (24) using equations (25). The reason is that the equality constraints associated to patch vertices can be redundant, and so one must first iterate over patch corner vertices $\mathbf{x}_c$, impose equality of all coefficients $\alpha_{\mathbf{j}}^{(k)}$ such that $B_{\mathbf{j},\mathbf{d}}^{(k)}(\mathbf{x}_c) \neq 0$, and only then iterate over edges, discarding the first and last scalar equations in (25) (the ones related to vertices) when adjoining them to (24).

An alternative approach to non-conforming continuity constraints, based on knot removal instead of knot insertion, is the following. Let $T \setminus T'$ be the set difference of two knot vectors, taking knot multiplicity into account. Then $T \cup T'$ can be decomposed as the disjoint union

$$T \cup T' = (T \setminus T') \cup (T \cap T') \cup (T' \setminus T). \tag{26}$$

For any edge $\mathcal{C}_{k,\ell}$, let $\mathbf{K}_{k,\ell}$ be the matrix that transforms a spline s in $S(T_i^{(k)}, d)$ as defined by its B-coefficients $\boldsymbol{\alpha}_{k,\ell}$ to a vector $\mathbf{K}_{k,\ell}\, \boldsymbol{\alpha}_{k,\ell}$ whose components are equal to the jumps in the derivatives of s from order $d - \mu + 1$ to $d - \nu$ at each node of $T_i^{(k)} \setminus T_j^{(\ell)}$, with μ being the node's multiplicity in $T_i^{(k)}$ and ν being the node's multiplicity in $T_j^{(\ell)}$ (possibly zero). The constraints $\mathbf{K}_{k,\ell}\, \boldsymbol{\alpha}_{k,\ell} = 0$ are known as *knot removal conditions*, and are equivalent to the inclusion $s \in S(T_i^{(k)} \cap T_j^{(\ell)}, d)$. It is appropriate to normalize each row of $\mathbf{K}_{k,\ell}$, for example with respect to the infinity norm, to ensure that the system matrix A is well-conditioned.

For any given edge $\mathcal{C}_{k,\ell}$, let $\mathbf{C}_{k,\ell}$ be the collocation matrix that transforms a spline s in $S(T_i^{(k)}, d)$ as defined by its B-coefficients $\boldsymbol{\alpha}_{k,\ell}$ to a vector $\mathbf{C}_{k,\ell}\, \boldsymbol{\alpha}_{k,\ell}$ whose components are equal to the values of s at the Greville abscissas $\hat{G}(T_i^{(k)} \cap T_j^{(\ell)}, d)$, endpoints excluded. Since any two splines $s, s' \in S(T_i^{(k)} \cap T_j^{(\ell)}, d)$ are equal if and only if they take the same values on the set of Greville abscissas (endpoints included), C^0 non-conforming joints can be achieved by the following two-step procedure. First, iterate over all patch corner vertices $\mathbf{x}_c$ and impose equality of every $\alpha_{\mathbf{j}}^{(k)}$ such that $B_{\mathbf{j},\mathbf{d}}^{\mathbf{T}^{(k)}}(\mathbf{x}_c) \neq 0$. Second, iterate over all patch edges $\mathcal{C}_{k,\ell}$ and for each impose the constraints

$$\mathbf{K}_{k,\ell}\, \boldsymbol{\alpha}_{k,\ell} = 0, \qquad \mathbf{C}_{k,\ell}\, \boldsymbol{\alpha}_{k,\ell} - \mathbf{C}_{\ell,k}\, \boldsymbol{\alpha}_{\ell,k} = 0, \qquad \mathbf{K}_{\ell,k}\, \boldsymbol{\alpha}_{\ell,k} = 0, \tag{27}$$

which can overall be understood as a decoupled version of equation (25). In fact, the approach based on knot removal conditions leads to a sparser and more structured matrix A in the final linear system to be solved. A comparison of the two approaches based on e.g. the condition number of A is beyond the scope of this paper.

Proposition 1. *Matrix A, formed by adjoining the non-conforming continuity constraints to the collocation conditions in A_{coll}, is a square matrix. Moreover, if the collocation conditions in A_{coll} are replaced by evaluation of the B-splines at the same list of points as in (24), i.e., to solve an interpolation problem instead of the conventional boundary integral equations (8) or (10), the resulting matrix A is nonsingular.*

Proof. See Appendix B. □

Remark 1. The previous proposition is meant to explain the choice of collocation points in the non-conforming setting and to provide a motivation for the proposed collocation conditions. However, nonsingularity of A for the solution of conventional boundary integral equations (8) or (10) is a much harder statement to prove, as the current theoretical understanding of collocation methods in the literature lags behind that of other methods (like Galerkin schemes), and so one cannot obtain the proof as a straightforward extension of the existing theory.

In fact, invertibility of A in the considered setting is still an open problem even in the simpler cases of inter-patch discontinuous spaces (Section 3.1) and inter-patch conforming continuous spaces (Section 3.2). Nevertheless, invertibility of the interpolation matrix is a necessary condition for collocation schemes to be profitably seen as projection methods in the sense of [22] and [26]: this point of view could provide a path towards a convergence proof for the considered scheme, as was done for example in [27] in a similar setting. To provide at least empirical evidence of nonsingularity of A, a survey of its condition number is done in Section 5 for different values of h, different kinds of inter-patch space continuity requirements, and different kinds of boundary conditions on a sphere.

4. Quadratures

4.1. Singularity extraction

Let us introduce a numerical integration method, which makes a function-by-function assembly phase possible. For the sake of simplicity, only the one-patch setting is considered ($M = 1$) when the source point and the integration domain belong to the same patch, thus avoiding any reference to the patch index. Some considerations about integration in the more general multi-patch setting are also given.

It is convenient to write the two singular kernels $\mathcal{G}_\kappa$ and $\partial\mathcal{G}_\kappa/\partial\mathbf{n}_\mathbf{y}$ as in (6) and (7) and analyze which terms are singular, hence a singular integration has to be considered, and which terms define regular

integrals. Referring to Appendix A for some explicit insights, as already noted in Section 2, the real part in (6) is weakly singular at $r = 0$ with its non-singular part $\cos(\kappa r)$ smooth under the assumption of a smooth geometry parameterization. For the same reason, its imaginary part is a smooth function. Similarly, the factor $\mathbf{r} \cdot \mathbf{n}_\mathbf{y}/r^3$ of the real part in (7) is weakly singular, while the other factor, $(\cos(\kappa r) + \kappa \sin(\kappa r)r)$, is smooth. Finally, the imaginary part in (7) is in general only C^1 continuous at $r = 0$ because the factor $\mathbf{r} \cdot \mathbf{n}_\mathbf{y}/r^2$ is bounded and $(\sin(\kappa r)/r - \kappa \cos(\kappa r))$ has a double zero at $r = 0$. In these numerical experiments such smoothness of the integrands was sufficient to numerically integrate the corresponding integrals with the required accuracy.

Remark 2. To improve accuracy of the numerical integration for integrals involving the imaginary part of (7), a more sophisticated approach could be considered. For example, the integrals could be handled similarly as the singular ones, treating the part $\mathbf{r} \cdot \mathbf{n}_\mathbf{y}/r^2$ as the "less regular part" of the integrand, since the remaining part $(\sin(\kappa r)/r - \kappa \cos(\kappa r))$ is an analytic function.

Let $\mathbf{s} \in [0,1]^2$ denote the preimage in the parametric domain of a fixed generic collocation point $\mathbf{x}$. Note that for brevity the patch index is referred to only when essential. Conversely, a superscript symbol $\tilde{}$ is adopted to refer to the patch scaling introduced at the end of Section 3.1. For example, $\tilde{\mathbf{x}} = \tilde{\mathbf{F}}(\mathbf{s})$ denotes the scaled $\mathbf{x} = \mathbf{F}(\mathbf{s})$, assuming that the considered scaling is that associated with the patch where the integration is developed. Then, let us introduce the following general form representing any integral to be dealt with,

$$\int_{R_\mathbf{j}} U(\mathbf{s},\mathbf{t}) \hat{B}_{\mathbf{j},\mathbf{d}}(\mathbf{t})\ g(\mathbf{t})\, d\mathbf{t}, \tag{28}$$

where g is a given smooth function, $\hat{B}_{\mathbf{j},\mathbf{d}}$ is a B-spline basis function, $R_\mathbf{j} := \mathrm{supp}\{\hat{B}_{\mathbf{j},\mathbf{d}}\}$ and U refers to any of the following two weakly singular kernels respectively associated with the single and double layer potential,

$$U(\mathbf{s},\mathbf{t}) = U_{\mathrm{SL}}(\mathbf{s},\mathbf{t}) := \frac{1}{\|\tilde{\mathbf{F}}(\mathbf{s}) - \tilde{\mathbf{F}}(\mathbf{t})\|_2} \quad \text{and}$$
$$U(\mathbf{s},\mathbf{t}) = U_{\mathrm{DL}}(\mathbf{s},\mathbf{t}) := \frac{(\tilde{\mathbf{F}}(\mathbf{s}) - \tilde{\mathbf{F}}(\mathbf{t})) \cdot \tilde{\boldsymbol{\nu}}(\mathbf{t})}{\|\tilde{\mathbf{F}}(\mathbf{s}) - \tilde{\mathbf{F}}(\mathbf{t})\|_2^3}, \tag{29}$$

with $\tilde{\boldsymbol{\nu}}(\mathbf{t}) := (\partial\tilde{\mathbf{F}}/\partial t_1)(\mathbf{t}) \times (\partial\tilde{\mathbf{F}}/\partial t_2)(\mathbf{t})$ and $\tilde{\mathbf{F}}$ denoting the scaled normal and the scaled mapping associated to the conformally scaled surface patch.

Remark 3. Integrals defining the entries of $\boldsymbol{\beta}$ do not include the basis functions $\hat{B}_{\mathbf{j},\mathbf{d}}$ directly. To split the integration domain $[0,1]^2$ into smaller subdomains and arrive to the above general form, additional knot vectors $T_{\mathrm{r},1}, T_{\mathrm{r},2}$ are introduced, and inside (17) and (19) a sum of all B-spline basis functions $\hat{B}_{\mathbf{j},\mathbf{0}}$ of degree zero, defined on $T_{\mathrm{r},1} \times T_{\mathrm{r},2}$, is added. Therefore, the approach to evaluate integrals in $\boldsymbol{\beta}$ is analogous to the one for the system matrix A.

It is easy to determine when the integral in (28) is actually singular. Indeed, since smooth surfaces without self-intersections are considered, this occurs if and only if $\tilde{\mathbf{x}}$ belongs to the scaled patch where the integration is developed, and the associated $\mathbf{s}$ belongs to $R_\mathbf{j}$. However, detection of nearly singular integrals that require analogous treatment is a more delicate task, in order to preserve the accuracy of the numerical scheme without deteriorating its efficiency. In such setting let the integral in (28) be nearly singular, when

$$\tilde{r}_{\min,\mathbf{j}}(\mathbf{s}) := \min_{\mathbf{t}\in R_\mathbf{j}} \|\tilde{\mathbf{F}}(\mathbf{s}) - \tilde{\mathbf{F}}(\mathbf{t})\|_2 \le c_u\ \delta, \tag{30}$$

where $0 < c_u < 1$ is a user-defined constant and δ is a suitable patch-depended threshold. For further details concerning the definition of δ see the discussion in Section 4.6.

When the condition (30) is not satisfied, the kernel U is considered regular and integration rules for regular integrals are applied. Conversely, when the kernel U in (28) is weakly singular or nearly singular, a regularization technique based on the subtraction of singularity is preliminarily adopted,

$$\int_{R_\mathbf{j}} U(\mathbf{s},\mathbf{t}) \hat{B}_{\mathbf{j},\mathbf{d}}(\mathbf{t}) g(\mathbf{t})\, d\mathbf{t} = \int_{R_\mathbf{j}} \left(U(\mathbf{s},\mathbf{t}) - U_\mathbf{s}^m(\mathbf{s}-\mathbf{t})\right) \hat{B}_{\mathbf{j},\mathbf{d}}(\mathbf{t}) g(\mathbf{t})\, d\mathbf{t} + \int_{R_\mathbf{j}} U_\mathbf{s}^m(\mathbf{s}-\mathbf{t}) \hat{B}_{\mathbf{j},\mathbf{d}}(\mathbf{t}) g(\mathbf{t})\, d\mathbf{t}, \tag{31}$$

where $U_\mathbf{s}^m$ is an approximation of $U(\mathbf{s},\bullet)$, obtained by truncating a particular series expansion of U about the singular point $\mathbf{t} = \mathbf{s}$ after the m-th term; see [17] for the first application of these expansions in the simplest form and [19] for detailed construction and analysis. Note that the singularity subtraction technique that splits an integral into two ones is applied only to a small portion of integrals. In this case, the first term of the right hand side of (31) becomes a *regularized integral* while the second one is a singular integral with a simplified singular kernel. The continuity of the integrand in the regularized integral is controlled by the number m of terms in $U_\mathbf{s}^m$ and is equal to C^{m-2} at $\mathbf{t} = \mathbf{s}$ for the chosen $m \ge 1$ (C^{-1} denotes functions that are integrable in the standard sense but have discontinuities of the first kind at $\mathbf{t} = \mathbf{s}$), if the geometry map $\mathbf{F}$ is a smooth enough function [19].

By defining local coordinates $\mathbf{z} := \mathbf{s} - \mathbf{t}$, the kernel reads

$$U_\mathbf{s}^m(\mathbf{z}) = \sum_{k=1}^{m} R_\mathbf{s}(\mathbf{z})^{-2(k+\gamma)+1}\ P_{\mathbf{s},3k+2\gamma-3}^{[k]}(\mathbf{z}), \tag{32}$$

where $R_\mathbf{s}(\mathbf{z}) := \sqrt{\mathbf{z}^\top M_\mathbf{s} \mathbf{z}}$ is a square root of a bivariate quadratic homogeneous polynomial and $M_\mathbf{s}$ is the 2×2 symmetric positive definite matrix associated with the first fundamental form of a smooth surface (e.g., see formulas (61) and (62) in Appendix A), $P_{\mathbf{s},3k+2\gamma-3}^{[k]}$ are suitable homogeneous polynomials of degrees $3k + 2\gamma - 3$, and $\gamma = 0$ and $\gamma = 1$ for $\mathcal{G}_\kappa$ and $\partial\mathcal{G}_\kappa/\partial\mathbf{n}_\mathbf{y}$, respectively. Note that coefficients inside $R_\mathbf{s}$ and $P_{\mathbf{s},3k+2\gamma-3}^{[k]}$ depend on a chosen $\mathbf{s}$ and on derivatives of the map $\tilde{\mathbf{F}}$. For example, for $m = 1$ the kernels of the single and double layer potentials are approximated as follows,

$$U_\mathbf{s}^1(\mathbf{z}) = \begin{cases} \frac{1}{4\pi}\left[R_\mathbf{s}(\mathbf{z})^{-1}\right] & \text{if } U = U_{\mathrm{SL}}, \\ \frac{1}{4\pi}\left[R_\mathbf{s}(\mathbf{z})^{-3} P_{\mathbf{s},2}^{[1]}(\mathbf{z})\right] & \text{if } U = U_{\mathrm{DL}}, \end{cases}$$

where $P_{\mathbf{s},2}^{[1]}(\mathbf{z}) = \frac{1}{2}\left(L\ z_1^2 + 2M\ z_1 z_2 + N z_2^2\right)$, and L, M, N are the coefficients of the second fundamental form of the geometry, evaluated at $\mathbf{s}$, see (61) in Appendix A.

Relating to the more general multi-patch setting, when source point $\mathbf{x} = \mathbf{F}^{(k)}(\mathbf{s})$ and integration variable $\mathbf{y} = \mathbf{F}^{(\ell)}(\mathbf{t})$ belong to different adjacent patches, $\Gamma^{(k)}$ and $\Gamma^{(\ell)}$, the integral in (28) is nearly singular if condition (30) is satisfied for involved points $\tilde{\mathbf{F}}^{(k)}(\mathbf{s}), \tilde{\mathbf{F}}^{(\ell)}(\mathbf{t})$, and regular otherwise. In the latter case, the procedure for regular integrals on one patch is adopted, while the former case clearly poses an additional challenge. In order to explain the procedure in such setting, a more precise notation is need to distinguish between the two involved patches $k \ne \ell$; the kernel U and its variations are equipped with superscript (k,ℓ), $U \to U^{(k,\ell)}$,

$$U_{\mathrm{SL}}^{(k,\ell)}(\mathbf{s},\mathbf{t}) := \frac{1}{\|\tilde{\mathbf{F}}^{(k)}(\mathbf{s}) - \tilde{\mathbf{F}}^{(\ell)}(\mathbf{t})\|_2},$$
$$U_{\mathrm{DL}}^{(k,\ell)}(\mathbf{s},\mathbf{t}) := \frac{(\tilde{\mathbf{F}}^{(k)}(\mathbf{s}) - \tilde{\mathbf{F}}^{(\ell)}(\mathbf{t})) \cdot \tilde{\boldsymbol{\nu}}^{(\ell)}(\mathbf{t})}{\|\tilde{\mathbf{F}}^{(k)}(\mathbf{s}) - \tilde{\mathbf{F}}^{(\ell)}(\mathbf{t})\|_2^3}, \tag{33}$$

indicating that the source point $\tilde{\mathbf{x}}$ is connected with $\mathbf{s}$ in the parametric domain via the geometry map $\tilde{\mathbf{F}}^{(k)}$ but integration is performed on the ℓ-th patch. Since the parameterization of the geometry is prescribed patch-wisely, the proposed series expansion $U_\mathbf{s}^{(k,\ell),m}$ is limited

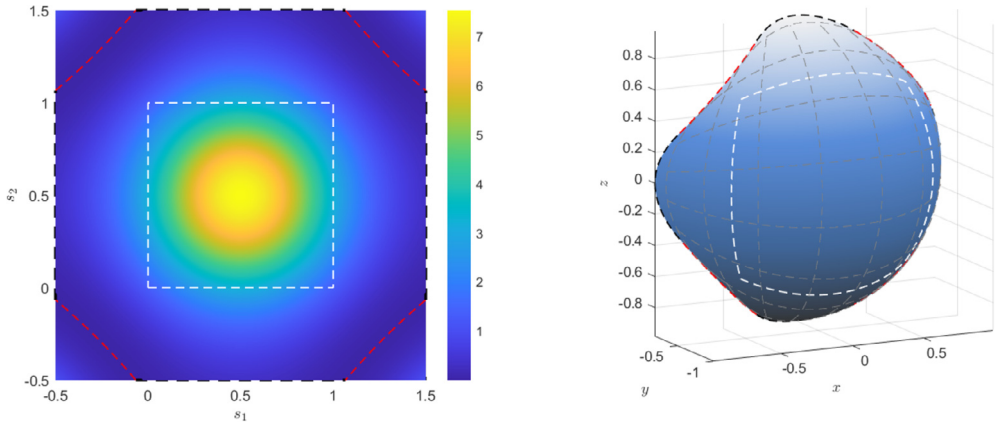

(a) Plot of $\det(M_{\mathbf{s}})$ (b) Extended patch

Fig. 1. An example of a spherical patch $\Gamma^{(\ell)}$ extension in the parametric and the physical domain. White lines indicate boundaries of the original patch. Red curves correspond to points, where $\det(M_{\mathbf{s}}) = 0$ and the parametrization is no longer regular. On the right isolines of the patch are depicted in grey.

to the k-th patch. To overcome this limitation, the function $\mathbf{F}^{(\ell)}$ is locally smoothly extended to a slightly larger domain, where a suitable approximation of the collocation point is found and used to develop the mentioned expansion. It is adequate to extend just the restriction of $\mathbf{F}^{(\ell)}$ sufficiently smoothly to a cell nearest to $\mathbf{x}$. Such a restriction can be easily converted in rational Bézier form (it can be easily obtained by performing a standard Bézier extraction algorithm), which is well defined and regular also slightly outside its original parametric domain $[0,1]^2$. The proposed extension is natural and reasonable for smooth inter-patch contacts, hence it is opted over other common more sophisticated but more expensive alternatives for surface extrapolations. With the proposed approach, function evaluations can be readily performed by standard algorithms, such as de Casteljau algorithm.

For simplicity of notation, let us denote with D_ℓ the locally extended parametric domain and let us use the same notation for the extended function, $\mathbf{F}^{(\ell)} : [0,1]^2 \subset D_\ell \to \mathbb{R}^3$, where clearly on the enlarged part of the domain the map $\mathbf{F}^{(\ell)}$ describes just an approximation of the actual geometry, which is exactly described by $\mathbf{F}^{(k)}$. By replacing $\tilde{\mathbf{x}} = \tilde{\mathbf{F}}^{(k)}(\mathbf{s})$ in (33) by $\tilde{\mathbf{F}}^{(\ell)}(\mathbf{s}_e)$ with

$$\mathbf{s}_e := \arg \min_{\mathbf{s}' \in D_\ell} \|\tilde{\mathbf{F}}^{(k)}(\mathbf{s}) - \tilde{\mathbf{F}}^{(\ell)}(\mathbf{s}')\|_2 , \tag{34}$$

the obtained kernel $U^{(\ell,\ell),m}_{\mathbf{s}_e}$ approximates $U^{(k,\ell),m}_{\mathbf{s}}$ and naturally generalizes the case $k = \ell$. Since $\tilde{\mathbf{F}}^{(k)}$ is assumed to be regular on $[0,1]^2$, the regularity is maintained also on D_ℓ for a sufficiently small extension, thus $M_{\mathbf{s}_e}$ in $R_{\mathbf{s}_e}$ is positive definite and $U^{(\ell,\ell),m}_{\mathbf{s}_e}$ is well defined for all $\mathbf{s}_e \in D_\ell$. Since the actual source point $\tilde{\mathbf{x}}$ is replaced by its nearby surrogate point $\tilde{\mathbf{F}}^{(\ell)}(\mathbf{s}_e)$, the cancellation of the singularity is not exact. This does not present any real problem because the source point lies outside the integration domain and the accuracy of singularity cancellation improves with smaller values of $\tilde{r}_{\min,\mathbf{j}}$; see Section 4.5 for the nearly singular numerical integration error analysis.

As an example, let $\Gamma^{(k)}$ and $\Gamma^{(\ell)}$ be two adjacent NURBS patches of a unit sphere, sharing a common edge, $\mathbf{F}^{(k)}(1,0) = \mathbf{F}^{(\ell)}(1,0)$, $\mathbf{F}^{(k)}(1,1) = \mathbf{F}^{(\ell)}(0,0)$ (see the beginning of Section 5 for more details on the geometry parametrization and Fig. 3(a) for visualization of the sphere representation). Note that in this setting each patch comprises only one mesh cell and can thus be extended in all directions in the parametric domain with just one Bézier form, e.g., on $[-\varepsilon, 1+\varepsilon]^2$ for $\varepsilon > 0$.

Let $\mathbf{x} = \mathbf{F}^{(k)}(\mathbf{s}) \in \Gamma^{(k)}$, $\mathbf{s} = (1-\varepsilon, 1-\varepsilon), (1-\varepsilon, 0.5)$, $\varepsilon = 10^{-6}$, be a collocation point near the vertex and near the centre of the interface of $\Gamma^{(\ell)}$, respectively (for simplicity let us assume $\mu_\ell = 1$). In Fig. 1 an extension of one spherical patch $\Gamma^{(\ell)}$ is depicted on extended domain $D_\ell = [-0.5, 1.5]^2$ – a much bigger domain extension than what is needed in practice. Function $\det(M_{\mathbf{s}}) = EG - F^2$ (E, F, G are coefficients of the first fundamental form of a smooth surface), a measure of regularity of the parametrization, is depicted in Fig. 1(a). Patch extension in the physical domain is shown in Fig. 1(b). In Fig. 2 the function $\mathbf{t} \mapsto |U^{(k,\ell)}(\mathbf{s},\mathbf{t}) - U^{(\ell,\ell),2}_{\mathbf{s}_e}(\mathbf{s}_e - \mathbf{t})|$ is depicted. Such function is the absolute value of the regularized part of the integrand in (31) for the kernels of the single and double layer potential. The figure shows its value in the parametric domain $[0,1]^2$ of $\Gamma^{(\ell)}$, together with the position of $\mathbf{s}_e$ in D_ℓ. The distance between the computed nearby surrogate point $\mathbf{F}^{(\ell)}(\mathbf{s}_e)$ and the actual source point $\mathbf{x} = \mathbf{F}^{(k)}(\mathbf{s})$ is approximately $1.2 \cdot 10^{-6}$ and $1.4 \cdot 10^{-6}$, when the source point is close to the vertex (left figures) and to the centre of the common interface (right figures), respectively. The figure shows that the regularized function $U^{(k,\ell)}(\mathbf{s},\mathbf{t}) - U^{(\ell,\ell),2}_{\mathbf{s}_e}(\mathbf{s}_e - \mathbf{t})$ has small oscillations and is bounded – in contrast, the maximum value of the function $\mathbf{t} \mapsto |U^{(k,\ell)}(\mathbf{s},\mathbf{t})|$ in $[0,1]^2$ is approximately $5.0 \cdot 10^5$ and $6.3 \cdot 10^5$ for the two cases with the single layer potential (top figures) and $8.7 \cdot 10^5$, $7.1 \cdot 10^5$ for the cases with the double layer potential (bottom figures). The presented example demonstrates that the regularized integrals can effectively be incorporated in routines for regular integrals presented in Section 4.3.

4.2. B-spline quasi-interpolation scheme

To approximate integrals in 3D collocation BEM, the 2D Quasi Interpolation (QI) scheme is utilized, firstly introduced in [28] for the tensor-product extension of the univariate Hermite QI scheme introduced in [29]. With such approach a bivariate function f is approximated on a rectangle R by using a QI spline tensor product operator $f \to \sigma_f := \sum_{\mathbf{i} \in \mathcal{J}^{\boldsymbol{\Theta}}} \lambda_{\mathbf{i}} \hat{B}^{\boldsymbol{\Theta}}_{\mathbf{i},\mathbf{p}}$, where $\{\hat{B}^{\boldsymbol{\Theta}}_{\mathbf{i},\mathbf{p}}, \mathbf{i} \in \mathcal{J}^{\boldsymbol{\Theta}}\}$ is the tensor-product B-spline basis generating the chosen finite dimensional space of splines defined on R and knot array $\boldsymbol{\Theta}$, with $\mathcal{J}^{\boldsymbol{\Theta}}$ denoting a local set of multi-indices used to identify the basis elements. In the considered QI scheme each coefficient $\lambda_{\mathbf{i}}, \mathbf{i} \in \mathcal{J}^{\boldsymbol{\Theta}}$, is computed as a linear combination of the values assumed in a suitable local subset of breakpoints by f, by both its first partial derivatives and also by its second mixed derivative, see [28] for details. However, in the present work a derivative-free variant of such QI scheme is considered, which is more suitable for numerical integration. Such variant is obtained by approximating the required derivative values with suitable finite difference formulas. Then, collecting all the coefficients $\lambda_{\mathbf{i}}, \mathbf{i} \in \mathcal{J}_R$, in a vector $\boldsymbol{\Lambda}$ in lexicographical order, a compact matrix notation reads

$$\boldsymbol{\Lambda} = \left(\hat{C}^{(p)}\right)^{\top} \mathbf{f} , \tag{35}$$

where $\mathbf{f}$ is a vector collecting with the same ordering all the values of f at the breakpoints and

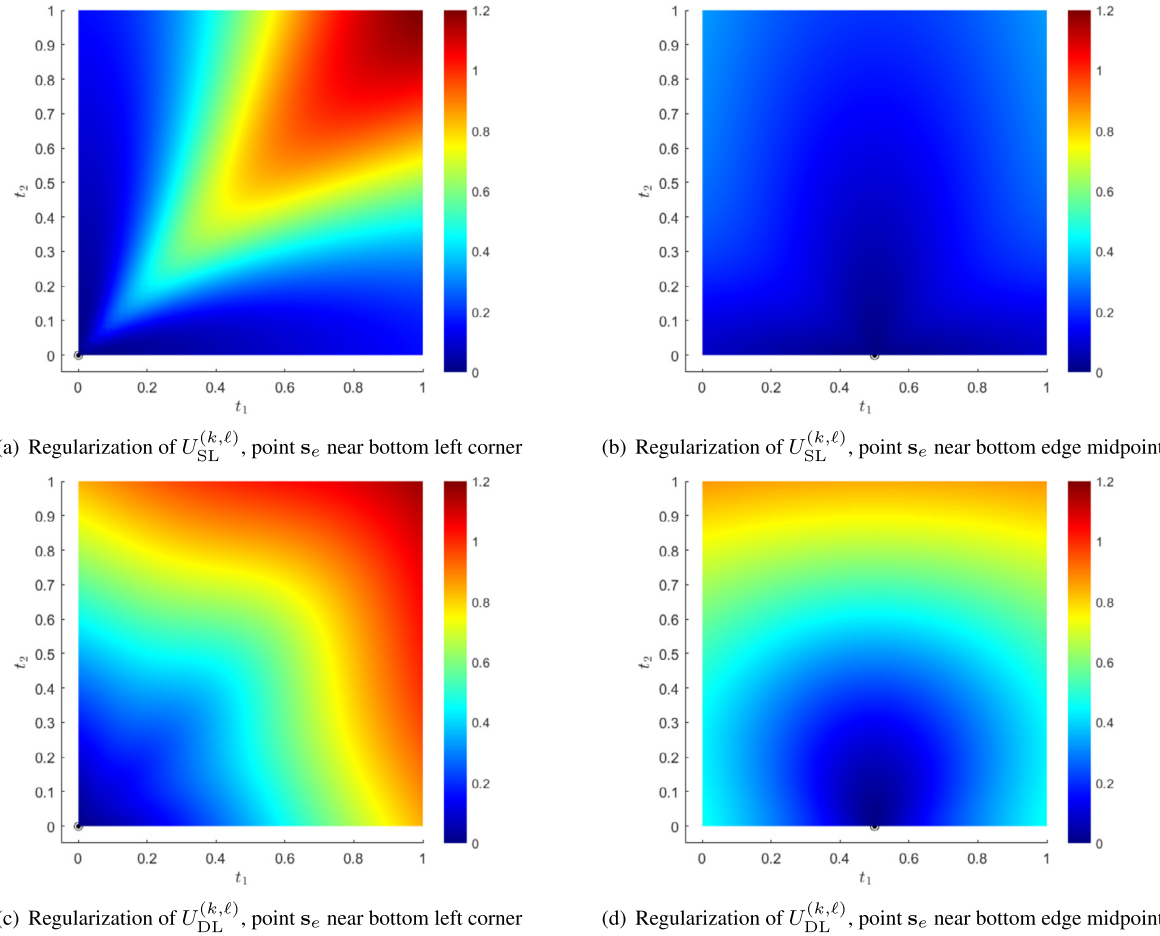

(a) Regularization of $U_{\mathrm{SL}}^{(k,\ell)}$, point $\mathbf{s}_e$ near bottom left corner

(b) Regularization of $U_{\mathrm{SL}}^{(k,\ell)}$, point $\mathbf{s}_e$ near bottom edge midpoint

(c) Regularization of $U_{\mathrm{DL}}^{(k,\ell)}$, point $\mathbf{s}_e$ near bottom left corner

(d) Regularization of $U_{\mathrm{DL}}^{(k,\ell)}$, point $\mathbf{s}_e$ near bottom edge midpoint

Fig. 2. An example of the absolute value of the regularized function of the nearly singular kernel with the source point and integration domain belonging to two different adjacent patches of a sphere. The points $\mathbf{s}_e$ are represented as a black dots.

$$\hat{C}^{(p)} := \big((\hat{A}_2^{\top} \otimes \hat{A}_1^{\top}) - (\hat{A}_2^{\top} \otimes (\hat{B}_1^{\top} D_{t_1})) - ((\hat{B}_2^{\top} D_{t_2}) \otimes \hat{A}_1^{\top}) + ((\hat{B}_2^{\top} D_{t_2}) \otimes (\hat{B}_1^{\top} D_{t_1}))\big)^{\top}. \tag{36}$$

In the above formula $\hat{A}_i$, $\hat{B}_i$ denote the two banded matrices, explicitly reported for example in [30], which are associated to the univariate original Hermite scheme formulated in the i-th direction, $i = 1, 2$; D_{t_i} are the matrices associated with the two analogous directional finite difference formulas used by the considered QI variant of the original scheme for approximating the first partial derivatives. Clearly, by incorporating a sufficiently accurate finite differences formula to approximate the required derivatives, the resulting derivative-free QI scheme shares the approximation power with the original scheme. On this concern, referring to the considered case with uniform breakpoints on R, for sufficiently smooth functions the following error bound can be easily derived from Theorem 1 reported in [28],[2]

$$\begin{aligned}\|f - \sigma_f\|_{\infty,R} \leq\, & v_1 \|\partial^{p_1+1,0} f\|_{\infty,R} \left(\frac{H_1}{\nu_1 - 1}\right)^{p_1+1} \\ & + v_2 \|\partial^{0,p_2+1} f\|_{\infty,R} \left(\frac{H_2}{\nu_2 - 1}\right)^{p_2+1} \\ & + v_3 \|\partial^{p_1+1,p_2+1} f\|_{\infty,R} \left(\frac{H_1}{\nu_1 - 1}\right)^{p_1+1} \left(\frac{H_2}{\nu_2 - 1}\right)^{p_2+1},\end{aligned} \tag{37}$$

where H_i and ν_i respectively denote the size of R and the number of uniform breakpoints in the i-th coordinate direction, $i = 1, 2$, $\partial^{i_1,i_2} f$ stands for $\partial^{i_1+i_2} f / (\partial t_1^{i_1} \partial t_2^{i_2})$ and in our setting the constants v_1, v_2 and v_3 just depend on $\mathbf{p}$. Thus the convergence order of the scheme with respect to $\max\{H_1, H_2\} \to 0$ but also to $\max\{(\nu_1 - 1)^{-1}, (\nu_2 - 1)^{-1}\}$ is equal to $\min\{p_1, p_2\} + 1$.

4.3. B-spline quadrature rules for regular integrals

Since in the assayed BIEs the regular integrands consist of the product between a bivariate regular function f with a tensor product B-spline $\hat{B}_{\mathbf{j},\mathbf{d}}$, a quadrature rule for the following integral is needed:

$$\int_{R_{\mathbf{j}}} f(\mathbf{t}) \hat{B}_{\mathbf{j},\mathbf{d}}(\mathbf{t})\, d\mathbf{t}. \tag{38}$$

Function f is approximated with the previously described QI scheme,

$$f \approx \sigma_f = \sum_{\mathbf{i} \in \mathcal{J}^{\boldsymbol{\Theta}_{\mathbf{j}}}} \lambda_{\mathbf{i}} \hat{B}_{\mathbf{i},\mathbf{p}}^{\boldsymbol{\Theta}_{\mathbf{j}}},$$

where $\hat{B}_{\mathbf{i},\mathbf{p}}^{\boldsymbol{\Theta}_{\mathbf{j}}}$ denotes a tensor product B-splines of bi-degree $\mathbf{p} = (p_1, p_2)$, ranging over a suitable multi-index set $\mathcal{J}^{\boldsymbol{\Theta}_{\mathbf{j}}}$, forming a local spline space on $R_{\mathbf{j}}$. Hence

$$\int_{R_{\mathbf{j}}} f(\mathbf{t}) \hat{B}_{\mathbf{j},\mathbf{d}}(\mathbf{t})\, d\mathbf{t} \approx \int_{R_{\mathbf{j}}} \sigma_f(\mathbf{t}) \hat{B}_{\mathbf{j},\mathbf{d}}(\mathbf{t})\, d\mathbf{t}. \tag{39}$$

[2] In the reference the theorem is formulated for hierarchical spline spaces, hence the case of the tensor product spline spaces is included with admissible class $m = 1$.

The product $\sigma_f \hat{B}_{\mathbf{j},\mathbf{d}}$ is a new spline that can be expressed in terms of another B-spline basis $\hat{B}^{\mathbf{\Pi_j}}_{\mathbf{k},\mathbf{p}+\mathbf{d}}$, $\mathbf{k} \in \mathcal{J}^{\mathbf{\Pi_j}}$, defined in a suitable local "product" spline space of bi-degree $\mathbf{p}+\mathbf{d}$. The set $\mathcal{J}^{\mathbf{\Pi_j}}$ of $N^{\mathbf{\Pi_j}}$ distinct multi-indices naturally identify elements in a tensor-product B-spline basis on knot array $\mathbf{\Pi_j}$.

Generalizing the idea developed in [31,32] for the one-dimensional case, the coefficients of $\sigma_f \hat{B}_{\mathbf{j},\mathbf{d}}$ in the B-spline basis of the product space can be written as $G_{\mathbf{j}}^{\top}\mathbf{\Lambda}$, with $\mathbf{\Lambda}$ defined by QI as specified in (35). In the current bivariate setting the matrix $G_{\mathbf{j}}$ is defined as $G_{\mathbf{j}} := G^{(p_1,d_1)}_{j_1} \otimes G^{(p_2,d_2)}_{j_2}$, where $G^{(p_1,d_1)}_{j_1}$ and $G^{(p_2,d_2)}_{j_2}$ are suitable direction-wise coefficient matrices and $\mathbf{j} = (j_1, j_2)$; its dimension is equal to $|\mathcal{J}^{\mathbf{\Theta_j}}| \times N^{\mathbf{\Pi_j}}$. Thus, the integral in (39) can finally be evaluated as,

$$\int_{R_{\mathbf{j}}} f(\mathbf{t})\hat{B}_{\mathbf{j},\mathbf{d}}(\mathbf{t})d\mathbf{t} \approx \mathbf{v}^{\top}G_{\mathbf{j}}^{\top}\mathbf{\Lambda} = \mathbf{v}^{\top}G_{\mathbf{j}}^{\top}(\hat{C}^{(p)})^{\top}\mathbf{f},$$

where the matrix $\hat{C}^{(p)}$ is defined in (36) and $\mathbf{v}$ denotes a vector of suitable length collecting in lexicographical order the following integrals of each B-spline $\hat{B}^{\mathbf{\Pi_j}}_{\mathbf{k},\mathbf{p}+\mathbf{d}}$ of the basis of the local product spline space,

$$\int_{R_{\mathbf{j}}} \hat{B}^{\mathbf{\Pi_j}}_{\mathbf{k},\mathbf{p}+\mathbf{d}}(\mathbf{t})\,d\mathbf{t} = \frac{|\mathrm{supp}(\hat{B}^{\mathbf{\Pi_j}}_{\mathbf{k},\mathbf{p}+\mathbf{d}})|}{(p_1+d_1+1)(p_2+d_2+1)}, \qquad \mathbf{k} \in \mathcal{J}^{\mathbf{\Pi_j}}.$$

As already mentioned, the derived integration rule is the tensor product extension of a variant specific for integrals including a B-spline weight of the 1D quadrature formula introduced in [33]. Therefore, the error analysis developed in [33] can be easily extended to such variant and lifted to the tensor product setting. To be more concise, let us assume that a uniform distribution of quadrature nodes is used in each $R_{\mathbf{j}}$ (i.e., uniform breakpoints in the associated local spline space are used by the QI scheme), since this is the common setting in the numerical experiments. Assuming f to be a sufficiently smooth function, the quadrature error of the rule to approximate the integral in (38) is upper bounded by a positive constant times the following quantity,

$$\begin{aligned}\frac{H_{1,\mathbf{j}}H_{2,\mathbf{j}}}{(d_1+1)(d_2+1)}\Bigg\{ &\|\partial^{p_1+r_1+1,0}f\|_{\infty,R_{\mathbf{j}}}\left(\frac{H_{1,\mathbf{j}}}{\nu_1-1}\right)^{p_1+r_1+1} \\ &+ \|\partial^{0,p_2+r_2+1}f\|_{\infty,R_{\mathbf{j}}}\left(\frac{H_{2,\mathbf{j}}}{\nu_2-1}\right)^{p_2+r_2+1} \\ &+ \|\partial^{p_1+r_1+1,p_2+r_2+1}f\|_{\infty,R_{\mathbf{j}}}\left(\frac{H_{1,\mathbf{j}}}{\nu_1-1}\right)^{p_1+r_1+1} \\ &\times\left(\frac{H_{2,\mathbf{j}}}{\nu_2-1}\right)^{p_2+r_2+1}\Bigg\}, \end{aligned} \tag{40}$$

where $H_{i,\mathbf{j}}$ and ν_i respectively denote the size of $R_{\mathbf{j}}$ and the number of uniform quadrature nodes in the i-th coordinate direction, $i = 1,2$ and $r_i = 1(0)$ for p_i even (odd). For fixed numbers ν_i of nodes, the convergence order of the quadrature scheme with respect to $\max\{H_{1,\mathbf{j}}, H_{2,\mathbf{j}}\} \to 0$ is

$$C_1 \min\{H_{1,\mathbf{j}}^{p_1+r_1+3}, H_{1,\mathbf{j}}^{p_2+r_2+3}\},$$

if the quotient $H_{1,\mathbf{j}}/H_{2,\mathbf{j}}$ is bounded from below and from above by positive constants for all nested integration subdomains $R_{\mathbf{j}}$. The constant C_1 depends on norms of all the involved derivatives of f in (40) for the largest considered $R_{\mathbf{j}}$. For a fixed $R_{\mathbf{j}}$, the convergence order with respect to $\min\{\nu_1,\nu_2\}$ is equal to

$$\tilde{C}_1 \min\{(\nu_1-1)^{-p_1-r_1-1}, (\nu_2-1)^{-p_2-r_2-1}\},$$

where the positive constant $\tilde{C}_1$ depends also on constants $H_{i,\mathbf{j}}$ but not on ν_i.

4.3.1. Numerical test 1

The results of some numerical experiments confirming the developed analysis are presented in Table 1, where both absolute (Δ_R) and relative errors (ϵ_R) are reported together with the corresponding convergence orders (respectively o_{Δ_R} and o_{ϵ_R}). For completeness both these errors are given, since the experimental convergence order of one cannot be deduced from the other. Indeed, different integrals are considered on different rows of the table because the convergence behaviour of the rules is considered with respect to $\max\{H_1, H_2\}$, as it is of interest in the IgA-BEM setting, where conversely ν_1 and ν_2 are fixed. The reference "exact" integrals are computed with `integral2` function in Matlab, which uses an adaptive approach with bisection and the tensor product formulation of Kronrod rules [34]. To obtain sufficiently accurate values, a more expensive element-wise computation of the integral (i.e., as many calls to `integral2` as the number of elements in $R_{\mathbf{j}}$) is necessary. This indirectly confirms that the reduced regularity of the B-spline factor poses a problem for Gaussian rules and their variants like Kronrod rules, when they are not applied element-wisely.

The notation $\mathbf{F} : [0,1]^2 \to S^2$ refers to a quartic NURBS representation of a mapped quadrilateral patch covering one sixth of a unit sphere, see Section 5 for the details. Conformally, the corresponding infinitesimal area element is denoted as $J(\mathbf{t})$. The considered factor f appearing in (38) is the product between J and the real part of the kernel $4\pi\partial\mathcal{G}_\kappa/\partial\mathbf{n}_y(\mathbf{x}_R, \mathbf{F}(\mathbf{t}))$, where $\kappa = 2$ and $\mathbf{x}_R = \mathbf{F}((0.9, 0.9))$ is a source point on the patch close to one of its vertices. The B-spline factor $B_{\mathbf{j}}$ in (38) has bi-degree (d,d) with $d = 1,2,3$ and it is the central function of the B-spline basis associated to a uniform $n \times n$ partition of $[0,1]^2$, where $n = 2k+d+1, k = 1,\dots,4$. Indeed, for each k it is set $\mathbf{j} = (k+d+1, k+d+1)$. Note that with this selection of n and of $\mathbf{j}$ the considered integral is regular for each $k \geq 1$. The number of uniform quadrature points in $R_{\mathbf{j}}$ along each coordinate direction is chosen so that, besides the vertices of the elements, there are always two inner nodes in each element. This means that in $R_{\mathbf{j}}$ the global number of quadrature nodes is 7^2, 10^2, 13^2 respectively for $d = 1,2,3$. The bi-degree $\mathbf{p}$ of the QI spline operator is set to $(4,4)$, thus the expected convergence order of the absolute error is 8 independently of d. Clearly, the expected convergence order of the relative error is 6, which is also confirmed from the table. Note also that the accuracy does not substantially depend on d.

4.4. B-spline quadrature rules for singular and nearly singular integrals

Let us focus on the rules developed for the numerical approximation of the second addend on the right of (31), which involves the simplified singular kernel $U^m_{\mathbf{s}}(\mathbf{s}-\mathbf{t})$. The first step is analogous to that adopted for regular integrals, since g is approximated by σ_g using quasi-interpolation and then it is multiplied by $\hat{B}_{\mathbf{j},\mathbf{d}}$. Thus

$$\int_{R_{\mathbf{j}}} U^m_{\mathbf{s}}(\mathbf{s}-\mathbf{t})\hat{B}_{\mathbf{j},\mathbf{d}}(\mathbf{t})g(\mathbf{t})\,d\mathbf{t} \approx \int_{R_{\mathbf{j}}} U^m_{\mathbf{s}}(\mathbf{s}-\mathbf{t})\hat{B}_{\mathbf{j},\mathbf{d}}(\mathbf{t})\sigma_g(\mathbf{t})\,d\mathbf{t} = \mathbf{v}^{\top}G_{\mathbf{j}}^{\top}(\hat{C}^{(p)})^{\top}\mathbf{g}, \tag{41}$$

where $\mathbf{g}$ is the vector whose entries are the values of g used by the QI operator and $\mathbf{v}$ collects in a suitable order all the following integrals

$$\int_{R_{\mathbf{j}}} U^m_{\mathbf{s}}(\mathbf{s}-\mathbf{t})\hat{B}^{\mathbf{\Pi_j}}_{\mathbf{k},\mathbf{p}+\mathbf{d}}(\mathbf{t})\,d\mathbf{t}, \qquad \mathbf{k} \in \mathcal{J}^{\mathbf{\Pi_j}}. \tag{42}$$

To complete the definition of the quadrature rule, the exact expressions of the above integrals (42) are needed. Let

$$\begin{aligned} I^{q_1,q_2}_{r_1,r_2}(k_1,k_2) := &\int_{\tau^{(1)}_{k_1}}^{\tau^{(1)}_{k_1+r_1+1}}\int_{\tau^{(2)}_{k_2}}^{\tau^{(2)}_{k_2+r_2+1}} U^m_{\mathbf{s}}(\mathbf{s}-\mathbf{t})(t_1-s_1)^{q_1}(t_2-s_2)^{q_2} \\ &\times \hat{B}_{k_1,r_1}(t_1)\hat{B}_{k_2,r_2}(t_2)dt_1dt_2, \end{aligned}$$

Table 1
Quadrature absolute error (Δ_R), relative error (ϵ_R) and corresponding convergence orders with $\mathbf{p}=(4,4)$ for the regular integral (38) in Numerical test 1.

k	$d=1$				$d=2$				$d=3$			
	Δ_R	o_{Δ_R}	ϵ_R	o_{ϵ_R}	Δ_R	o_{Δ_R}	ϵ_R	o_{ϵ_R}	Δ_R	o_{Δ_R}	ϵ_R	o_{ϵ_R}
1	1.63e-06	–	1.02e-05	–	4.71e-07	–	4.60e-06	–	3.02e-06	–	4.23e-05	–
2	5.99e-08	8.1	8.19e-07	6.2	2.84e-08	8.3	5.31e-07	6.4	1.47e-08	10.5	3.58e-07	16.5
3	5.98e-09	8.0	1.44e-07	6.0	3.54e-09	8.3	1.08e-07	6.3	2.08e-09	8.8	7.84e-08	6.8
4	1.01e-09	8.0	3.76e-08	6.0	6.82e-10	8.2	3.09e-08	6.2	4.35e-10	8.6	2.35e-08	6.6

where $\mathbf{k}=(k_1,k_2)$ and $\tau^{(\ell)}_{k_\ell+j}, j=0,\dots,r_\ell, \ell=1,2$ define the two univariate knot vectors active in the definition of $\hat{B}^{\pi}_{\mathbf{k},\mathbf{p}+\mathbf{d}}$, where for brevity let $r_\ell := p_\ell + d_\ell$, which is the univariate degree in the ℓ-th direction of the product space. Then, using the tensor product extension of the Cox-de Boor recurrence relation for B-splines [3], the expression $I^{q_1,q_2}_{r_1,r_2}(k_1,k_2)$ is a linear combination of $I^{q_1+m_1,q_2+m_2}_{r_1-1,r_2-1}(k_1+w_1,k_2+w_2)$, where $m_1,m_2,w_1,w_2=0,1$. Starting with $q_1=q_2=0$ and iterating this recurrence up to B-splines of degree 0 in both coordinate directions, the procedure can be completed, provided that the following *basic moments* have been preliminarily computed for q_ℓ and i_ℓ, respectively ranging in the set of indices $0,\dots,p_\ell+r_\ell$ and $k_\ell,\dots,k_\ell+r_\ell, \ell=1,2$,

$$I^{q_1,q_2}_{0,0}(i_1,i_2) = \int_{\tau^{(1)}_{i_1}}^{\tau^{(1)}_{i_1+1}}\int_{\tau^{(2)}_{i_2}}^{\tau^{(2)}_{i_2+1}} U^m_{\mathbf{s}}(\mathbf{s}-\mathbf{t})(t_1-s_1)^{q_1}(t_2-s_2)^{q_2}\,dt_1\,dt_2$$
$$= \int_{s_1-\tau^{(1)}_{i_1+1}}^{s_1-\tau^{(1)}_{i_1}}\int_{s_2-\tau^{(2)}_{i_2+1}}^{s_2-\tau^{(2)}_{i_2}} U^m_{\mathbf{s}}(\mathbf{z})(-z_1)^{q_1}(-z_2)^{q_2}\,dz_1\,dz_2.$$

This can be done by relying on the analytical expressions derived in [19] and computed with the help of Wolfram Mathematica software.

The next step is to derive the asymptotic accuracy of these rules with respect to the $\max\{H_{1,\mathbf{j}},H_{2,\mathbf{j}}\}\to 0$, where $H_{i,\mathbf{j}}$ denotes the size of the integration domain $R_{\mathbf{j}}$ in the i-th coordinate direction. From (41) it is easy to show that the absolute value of the related quadrature error can be upper bounded by

$$\|g-\sigma_g\|_{\infty,R_{\mathbf{j}}}\int_{R_{\mathbf{j}}}|U^m_{\mathbf{s}}(\mathbf{s}-\mathbf{t})|\,\hat{B}_{\mathbf{j},\mathbf{d}}(\mathbf{t})\,d\mathbf{t}. \tag{43}$$

Using the triangle inequality $|U^m_{\mathbf{s}}(\mathbf{s}-\mathbf{t})|\le|U(\mathbf{s},\mathbf{t})|+|U^m_{\mathbf{s}}(\mathbf{s}-\mathbf{t})-U(\mathbf{s},\mathbf{t})|$, the integral in (43) is bounded by a sum of two new integrals. Then, by applying Proposition 3 reported in Appendix A, the first integral is estimated as

$$\int_{R_{\mathbf{j}}}|U(\mathbf{s},\mathbf{t})|\,\hat{B}_{\mathbf{j},\mathbf{d}}(\mathbf{t})\,d\mathbf{t}\le\int_{R_{\mathbf{j}}}|U(\mathbf{s},\mathbf{t})|\,d\mathbf{t}\le C_2\max\{H_1,H_2\}. \tag{44}$$

The second integral involves a tail of the series expansion of $U(\mathbf{s},\bullet)$ about the source point $\mathbf{s}$. Referring to results in [19], there exists a positive constant C_3 involving the infinity norm of derivatives of $\tilde{\mathbf{F}}$ of degree $\le m$ on $R_{\mathbf{j}}$, such that

$$\|U^m_{\mathbf{s}}(\mathbf{s}-\mathbf{t})-U(\mathbf{s},\mathbf{t})\|_{\infty,R_{\mathbf{j}}}\le C_3\frac{\left(\max\{H_{1,\mathbf{j}},H_{2,\mathbf{j}}\}\right)^{m-1}}{m!},$$

hence

$$\int_{R_{\mathbf{j}}}|U^m_{\mathbf{s}}(\mathbf{s}-\mathbf{t})-U(\mathbf{s},\mathbf{t})|\,\hat{B}_{\mathbf{j},\mathbf{d}}(\mathbf{t})\,d\mathbf{t}\le C_3\frac{\left(\max\{H_{1,\mathbf{j}},H_{2,\mathbf{j}}\}\right)^{m}}{m!(d_1+1)(d_2+1)}. \tag{45}$$

By combining these estimates with the bound in (37) for the QI error, the following error bound for the singular integral in (41) is derived with respect to size of $R_{\mathbf{j}}$,

$$C\max\{H^{p_1+2}_{1,\mathbf{j}},H^{p_2+2}_{2,\mathbf{j}}\},$$

where $C=C_1\max\{C_2,C_3\}$ and C_1 contains norms of all the involved derivatives of $f=g-\sigma_g$ in (40) for the largest considered $R_{\mathbf{j}}$. Instead, by fixing domain $R_{\mathbf{j}}$, the error bound with respect to $\min\{\nu_1-1,\nu_2-1\}$ is equal to

$$\tilde{C}\max\{(\nu_1-1)^{-p_1-1},(\nu_2-1)^{-p_2-1}\},$$

where $\tilde{C}$ contains a corresponding constant $\tilde{C}_1$ to the one at the end of Section 4.3, involving the function $f=g-\sigma_g$, multiplied by right-hand side estimates of (44) and (45).

4.4.1. Numerical test 2

To confirm the developed theoretical analysis, numerical results of selected singular integrals are presented in Table 2 for both absolute (Δ_S) and relative errors (ϵ_S), together with the corresponding convergence orders (respectively o_{Δ_S} and o_{ϵ_S}). The experiment is essentially a repetition of Test 1, the difference being that $\mathbf{x}_R$ is replaced by $\mathbf{x}_S=\mathbf{F}((0.5,0.5))$; hence all the integrals are singular, since $(0.5,0.5)$ lies inside the integration domain $R_{\mathbf{j}}$. The "exact" integrals are evaluated element-wisely with the Matlab function `integral2`, with a possible preliminary rectangular splitting of the domain at $(0.5,0.5)$ (to place the singularity at a vertex of the integration domain) and by applying the standard Duffy transformation [35].

All integrals are split via the subtraction (31) with $m=2$; the regular part is computed with the rule for regular integrals, while the singular part that contains an approximate kernel is evaluated with the rule for singular integrals. The errors reported in the table are therefore accumulative errors of both integrations. The bi-degree $\mathbf{p}$ of the QI is set to $(2,2)$ and the number of uniformly spaced quadrature nodes is set to 5 and 2 in each coordinate direction inside each element (by not counting mesh knots) for the regular and singular integrals, respectively. Hence, the total number of quadrature nodes in $R_{\mathbf{j}}$ is set to $13^2,19^2,25^2$ for $d=1,2,3$, respectively, for the regular rule and $7^2,10^2,13^2$ for the singular one. A lower value for $\mathbf{p}$ for the regular rule than that adopted in Test 1 (and conversely selecting an increased number of quadrature nodes) is motivated by reduced regularity of first term on the right-hand side of (31). The results reported in Table 2 are roughly one order higher than the worst expected theoretical order 4 (for the absolute error) and 3 (for the relative error). Again, the results do not vary significantly with d.

4.5. Quadrature rules for inter-patch nearly singular integrals

Numerical integration of inter-patch nearly singular integrals is performed essentially the same as for (nearly) singular integrals, presented in the previous Section 4.4. The main difference is that the surrogate point $\tilde{\mathbf{F}}^{(\ell)}(\mathbf{s}_e)$, defined in (34), of the source point $\tilde{\mathbf{F}}^{(k)}(\mathbf{s})$ is used to define the approximate kernel $U^{(\ell,\ell),m}_{\mathbf{s}_e}$ for the singularity subtraction. For $U^{(k,\ell)}\in\{U^{(k,\ell)}_{\mathrm{SL}},U^{(k,\ell)}_{\mathrm{DL}}\}$ the nearly singular integral

$$\int_{R_j}U^{(k,\ell)}(\mathbf{s},\mathbf{t})\hat{B}_{\mathbf{j},\mathbf{d}}(\mathbf{t})g(\mathbf{t})d\mathbf{t}$$

is split into a sum of two integrals by writing the kernel as

$$U^{(k,\ell)}(\mathbf{s},\mathbf{t})=(U^{(k,\ell)}(\mathbf{s},\mathbf{t})-U^{(\ell,\ell),m}_{\mathbf{s}_e}(\mathbf{s}_e-\mathbf{t}))+U^{(\ell,\ell),m}_{\mathbf{s}_e}(\mathbf{s}_e-\mathbf{t}).$$

Table 2
Quadrature absolute error (Δ_S), relative error (ϵ_S) and corresponding convergence orders with $\mathbf{p}=(2,2)$ for the singular integrals (41) in Numerical test 2.

k	$d=1$				$d=2$				$d=3$			
	Δ_S	o_{Δ_S}	ϵ_S	o_{ϵ_S}	Δ_S	o_{Δ_S}	ϵ_S	o_{ϵ_S}	Δ_S	o_{Δ_S}	ϵ_S	o_{ϵ_S}
1	5.60e-04	–	8.76e-04	–	1.36e-04	–	3.30e-04	–	5.07e-05	–	1.68e-04	–
2	7.83e-05	4.9	1.87e-04	3.8	2.67e-05	4.8	9.21e-05	3.8	1.26e-05	4.8	5.63e-05	3.8
3	1.87e-05	5.0	6.00e-05	4.0	7.63e-06	5.0	3.41e-05	3.9	4.13e-06	5.0	2.33e-05	4.0
4	6.03e-06	5.1	2.43e-05	4.1	2.75e-06	5.1	1.50e-05	4.1	1.63e-06	5.1	1.11e-05	4.1

The second integral is singular with a simplified kernel $U^{(\ell,\ell),m}_{\mathbf{s}_e}$, hence it is evaluated with the rule for singular integrals in Section 4.4. The first integral is regular and the rule in Section 4.3 is employed.

Since the singularity cancellation is not exact for the inter-patch case, the error analysis of the rule rests upon the third order accuracy of the surrogate source point to the actual source point with respect to the distance to the integration point. A sketch of the proof of the latter property can be demonstrated as follows. Let the source point $\tilde{\mathbf{F}}^{(k)}(\mathbf{s})$ be fixed and let

$$\mathbf{t}^\star := \arg\min\{\|\tilde{\mathbf{F}}^{(k)}(\mathbf{s})-\tilde{\mathbf{F}}^{(\ell)}(\mathbf{t})\|_2 : \mathbf{t}\in\partial R_{\mathbf{j}}\}$$

be the argument of the closest point integration point to the source point. Let

$$\begin{aligned}\tilde{\mathbf{F}}^{(\ell)}(\mathbf{t}) = \tilde{\mathbf{F}}^{(\ell)}(\mathbf{t}^\star) &+ \mathbf{c}_{1,0}(t_1-t_1^\star)+\mathbf{c}_{0,1}(t_2-t_2^\star)\\ &+\mathbf{c}_{2,0}(t_1-t_1^\star)^2+\mathbf{c}_{1,1}(t_1-t_1^\star)(t_2-t_2^\star)+\mathbf{c}_{0,2}(t_2-t_2^\star)^2+O(\|\mathbf{t}-\mathbf{t}^\star\|^3)\end{aligned}$$

be the Taylor expansions of $\tilde{\mathbf{F}}^{(\ell)}$ of the patch $\Gamma^{(\ell)}$ parametrization about the point $\mathbf{t}^\star$. Let γ be a suitable regular reparametrization function such that a Taylor expansion for $\tilde{\mathbf{F}}^{(k)}\circ\gamma$ about $\mathbf{t}^\star$ is obtained, in the same parameter $\mathbf{t}$ as for $\tilde{\mathbf{F}}^{(\ell)}$:

$$\begin{aligned}(\tilde{\mathbf{F}}^{(k)}\circ\gamma)(\mathbf{t}) =& \tilde{\mathbf{F}}^{(\ell)}(\mathbf{t}^\star)+\mathbf{d}_{1,0}(t_1-t_1^\star)+\mathbf{d}_{0,1}(t_2-t_2^\star)\\ &+\mathbf{d}_{2,0}(t_1-t_1^\star)^2+\mathbf{d}_{1,1}(t_1-t_1^\star)(t_2-t_2^\star)+\mathbf{d}_{0,2}(t_2-t_2^\star)^2\\ &+O(\|\mathbf{t}-\mathbf{t}^\star\|^3).\end{aligned}$$

Since the geometry is assumed to be C^2 continuous across patch interfaces, it follows $\mathbf{c}_{i,j}=\mathbf{d}_{i,j}$ for $i+j\le 2$ and hence $\|(\tilde{\mathbf{F}}^{(k)}\circ\gamma)(\mathbf{t})-\tilde{\mathbf{F}}^{(\ell)}(\mathbf{t})\|_2 = O(\|\mathbf{t}-\mathbf{t}^\star\|_2^3)$. By setting suitable $\mathbf{t}$ and γ such that $\tilde{\mathbf{F}}^{(k)}(\mathbf{s})=(\tilde{\mathbf{F}}^{(k)}\circ\gamma)(\mathbf{t})$, the distance between the source point and its surrogate point $\tilde{\mathbf{F}}^{(\ell)}(\mathbf{s}_e)$ is bounded as

$$\|\tilde{\mathbf{F}}^{(k)}(\mathbf{s})-\tilde{\mathbf{F}}^{(\ell)}(\mathbf{s}_e)\|_2 \le \|(\tilde{\mathbf{F}}^{(k)}\circ\gamma)(\mathbf{t})-\tilde{\mathbf{F}}^{(\ell)}(\mathbf{t})\|_2 = O(\|\mathbf{t}-\mathbf{t}^\star\|_2^3). \tag{46}$$

To inherit convergence properties from the rule for regular integrals, it is sufficient to prove that $|U^{(k,\ell)}(\mathbf{s},\mathbf{t})-U^{(\ell,\ell),m}_{\mathbf{s}_e}(\mathbf{s}_e-\mathbf{t})|$ is bounded on $R_{\mathbf{j}}$ by a positive constant, no matter how close the source point $\tilde{\mathbf{F}}^{(k)}(\mathbf{s})$ is to the integration point $\tilde{\mathbf{F}}^{(\ell)}(\mathbf{t}^\star)$.

Using the triangle inequality it follows that

$$\begin{aligned}|U^{(k,\ell)}(\mathbf{s},\mathbf{t})-U^{(\ell,\ell),m}_{\mathbf{s}_e}(\mathbf{s}_e-\mathbf{t})| \le& |U^{(k,\ell)}(\mathbf{s},\mathbf{t})-U^{(\ell,\ell)}(\mathbf{s}_e,\mathbf{t})|\\ &+|U^{(\ell,\ell)}(\mathbf{s}_e,\mathbf{t})-U^{(\ell,\ell),m}_{\mathbf{s}_e}(\mathbf{s}_e-\mathbf{t})|.\end{aligned} \tag{47}$$

The second term in (47) is bounded for $m\ge 1$ [19].

To prove that the first term in (47) can be bounded, let us define the following quantities

$$\begin{aligned}\tilde{\mathbf{r}}_1(\mathbf{s}) &:= \tilde{\mathbf{F}}^{(k)}(\mathbf{s})-\tilde{\mathbf{F}}^{(\ell)}(\mathbf{t}^\star), & \tilde{r}_1(\mathbf{s}) &:= \|\tilde{\mathbf{r}}_1(\mathbf{s})\|_2,\\ \tilde{\mathbf{r}}_2(\mathbf{s}_e) &:= \tilde{\mathbf{F}}^{(\ell)}(\mathbf{s}_e)-\tilde{\mathbf{F}}^{(\ell)}(\mathbf{t}^\star), & \tilde{r}_2(\mathbf{s}_e) &:= \|\tilde{\mathbf{r}}_2(\mathbf{s}_e)\|_2,\\ \tilde{\mathbf{r}}(\mathbf{s},\mathbf{s}_e) &:= \tilde{\mathbf{F}}^{(k)}(\mathbf{s})-\tilde{\mathbf{F}}^{(\ell)}(\mathbf{s}_e), & \tilde{r}(\mathbf{s},\mathbf{s}_e) &:= \|\tilde{\mathbf{r}}(\mathbf{s},\mathbf{s}_e)\|_2,\end{aligned} \tag{48}$$

with the following assumption $\tilde{r}_1(\mathbf{s}),\tilde{r}_2(\mathbf{s}_e)=O(||\mathbf{t}-\mathbf{t}^\star||_2)$. By considering inequality (46) regarding the accuracy of the surrogate point, for $\tilde{\mathbf{F}}^{(k)}(\mathbf{s})$ sufficiently close to $\tilde{\mathbf{F}}^{(\ell)}(\mathbf{t}^\star)$, there exists a positive constant C_1 such that

$$\tilde{r}(\mathbf{s},\mathbf{s}_e)\le C_1\min\{\tilde{r}_1(\mathbf{s})^3,\tilde{r}_2(\mathbf{s}_e)^3\}.$$

Therefore, using the reverse triangle inequality and distances in (48), the term for the single layer potential is bounded as

$$\begin{aligned}|U^{(k,\ell)}_{\mathrm{SL}}(\mathbf{s},\mathbf{t}^\star)-U^{(\ell,\ell)}_{\mathrm{SL}}(\mathbf{s}_e,\mathbf{t}^\star)| &= \left|\frac{1}{\tilde{r}_1(\mathbf{s})}-\frac{1}{\tilde{r}_2(\mathbf{s}_e)}\right| = \frac{|\tilde{r}_2(\mathbf{s}_e)-\tilde{r}_1(\mathbf{s})|}{\tilde{r}_1(\mathbf{s})\tilde{r}_2(\mathbf{s}_e)}\\ &\le \frac{\tilde{r}(\mathbf{s},\mathbf{s}_e)}{\tilde{r}_1(\mathbf{s})\tilde{r}_2(\mathbf{s}_e)}\end{aligned}$$

that tends to zero, when the source point approaches the integration point.

In the case of the double layer potential use a triangle inequality,

$$\begin{aligned}|U^{(k,\ell)}_{\mathrm{DL}}(\mathbf{s},\mathbf{t}^\star)-U^{(\ell,\ell)}_{\mathrm{DL}}(\mathbf{s}_e,\mathbf{t}^\star)| &= \left|\frac{\tilde{\mathbf{r}}_1(\mathbf{s})\cdot\mathbf{n}}{\tilde{r}_1(\mathbf{s})^3}-\frac{\tilde{\mathbf{r}}_2(\mathbf{s}_e)\cdot\mathbf{n}}{\tilde{r}_2(\mathbf{s}_e)^3}\right|\\ &\le \left|\frac{\tilde{\mathbf{r}}_1(\mathbf{s})\cdot\mathbf{n}}{\tilde{r}_1(\mathbf{s})^3}-\frac{\tilde{\mathbf{r}}_1(\mathbf{s})\cdot\mathbf{n}}{\tilde{r}_2(\mathbf{s}_e)^3}\right|+\left|\frac{(\tilde{\mathbf{r}}_2(\mathbf{s}_e)-\tilde{\mathbf{r}}_1(\mathbf{s}))\cdot\mathbf{n}}{\tilde{r}_2(\mathbf{s}_e)^3}\right|.\end{aligned} \tag{49}$$

The bound for the first term in (49) is simplified to

$$\begin{aligned}\left|\frac{\tilde{\mathbf{r}}_1(\mathbf{s})\cdot\mathbf{n}}{\tilde{r}_1(\mathbf{s})^3}-\frac{\tilde{\mathbf{r}}_1(\mathbf{s})\cdot\mathbf{n}}{\tilde{r}_2(\mathbf{s}_e)^3}\right| &\le |\tilde{\mathbf{r}}_1(\mathbf{s})\cdot\mathbf{n}|\left|\frac{\tilde{r}_2(\mathbf{s}_e)^3-\tilde{r}_1(\mathbf{s})^3}{\tilde{r}_1(\mathbf{s})^3\tilde{r}_2(\mathbf{s}_e)^3}\right|\\ &= \frac{|\tilde{\mathbf{r}}_1(\mathbf{s})\cdot\mathbf{n}|}{\tilde{r}_1(\mathbf{s})^2}|\tilde{r}_2(\mathbf{s}_e)-\tilde{r}_1(\mathbf{s})|\frac{\tilde{r}_2(\mathbf{s}_e)^2+\tilde{r}_1(\mathbf{s})\tilde{r}_2(\mathbf{s}_e)+\tilde{r}_1(\mathbf{s})^2}{\tilde{r}_1(\mathbf{s})\tilde{r}_2(\mathbf{s}_e)^3}.\end{aligned} \tag{50}$$

The first term in (50) is bounded by applying Corollary 1 in Appendix A,

$$\frac{|\tilde{\mathbf{r}}_1(\mathbf{s})\cdot\mathbf{n}|}{\tilde{r}_1(\mathbf{s})^2}\le C_2$$

for some positive constant C_2. By applying again the reverse triangle inequality, the remaining part in (50) is bounded by a term

$$\tilde{r}(\mathbf{s},\mathbf{s}_e)\frac{3\max\{\tilde{r}_1(\mathbf{s})^2,\tilde{r}_2(\mathbf{s}_e)^2\}}{\min\{\tilde{r}_1(\mathbf{s})^4,\tilde{r}_2(\mathbf{s}_e)^4\}}\le 3C_1\frac{\max\{\tilde{r}_1(\mathbf{s})^2,\tilde{r}_2(\mathbf{s}_e)^2\}}{\min\{\tilde{r}_1(\mathbf{s}),\tilde{r}_2(\mathbf{s}_e)\}}. \tag{51}$$

From assumption $\tilde{r}_1(\mathbf{s}),\tilde{r}_2(\mathbf{s}_e)=O(||\mathbf{t}-\mathbf{t}^\star||_2)$ it directly follows $\max\{\tilde{r}_1(\mathbf{s}),\tilde{r}_2(\mathbf{s}_e)\}\le C_3\min\{\tilde{r}_1(\mathbf{s}),\tilde{r}_2(\mathbf{s}_e)\}$ for some $C_3>0$. Hence, the upper bound in (51) tends to zero, when the source point approaches the integration point.

The second term in (49) is bounded as

$$\left|\frac{(\tilde{\mathbf{r}}_2(\mathbf{s}_e)-\tilde{\mathbf{r}}_1(\mathbf{s}))\cdot\mathbf{n}}{\tilde{r}_2(\mathbf{s}_e)^3}\right| = \left|\frac{\tilde{\mathbf{r}}(\mathbf{s},\mathbf{s}_e)\cdot\mathbf{n}}{\tilde{r}_2(\mathbf{s}_e)^3}\right|\le\left|\frac{\tilde{r}(\mathbf{s},\mathbf{s}_e)}{\tilde{r}_2(\mathbf{s}_e)^3}\right|\le C_1.$$

4.6. The threshold for near singularity detection

The efficient and accurate evaluation of different types of integrals (28) appearing in the considered BIEs is crucial, see also [36] on such concern. To this aim, the interest in this subsection is in determining a reasonable threshold δ to be used in (30) to switch between nearly singular and regular integrals. The goal is to apply the error bound (40) introduced in Section 4.3 to $f=gU$, in order to derive on each patch a mesh dependent definition of the threshold δ to be used in (30).

By analyzing the nearly singular nature of the considered integral in (28), it is important to observe that the function $f:=gU(\mathbf{s},\bullet)$ for a fixed $\mathbf{s}=\tilde{\mathbf{F}}^{-1}(\tilde{\mathbf{x}})$ includes a factor proportional to $1/\tilde{r}$, where $\tilde{r}=\|\tilde{\mathbf{F}}(\mathbf{s})-\tilde{\mathbf{F}}(\bullet)\|_2$.

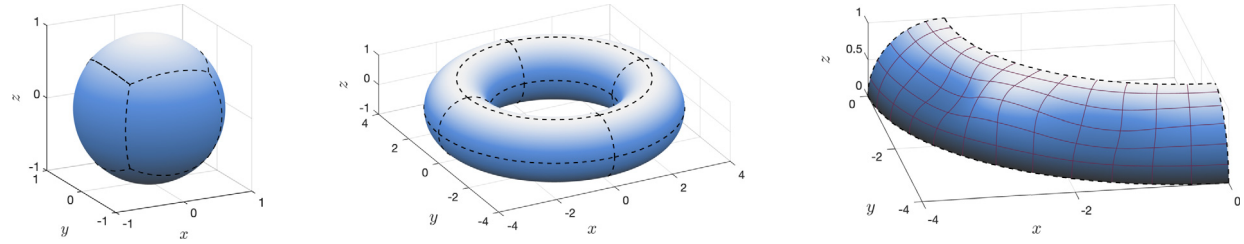

(a) 6-patch quartic NURBS representation of a sphere

(b) 16-patch quadratic NURBS representation of a torus

(c) Distorted quadratic torus patch. Selected isolines are shown in red to aid visualization.

Fig. 3. Exact NURBS representations of the geometries for the numerical tests. Scenes are lit from the positive z direction.

Hence, $\|\partial^{i_1,i_2} f\|_{\infty,R_{\mathbf{j}}}$ includes a term $\tilde{r}_{\min,\mathbf{j}}(\mathbf{s})^{-i_1-i_2-1}$, where $\tilde{r}_{\min,\mathbf{j}}(\mathbf{s})$ is the minimal distance between $\tilde{\mathbf{x}}$ and the physical integration domain image of $R_{\mathbf{j}}$ via the geometry map $\tilde{\mathbf{F}}$, see its definition in formula (30). Thus, considering the expression of the error bound in (40) for a fixed number of uniformly spaced quadrature nodes, a remarkable reduction of the convergence order with respect to $\max\{H_{1,\mathbf{j}}, H_{2,\mathbf{j}}\} \to 0$ would occur if $\tilde{r}_{\min,\mathbf{j}}(\mathbf{s})$ would reduce proportionally to it, due to increasing terms "$\|\partial^{i_1,i_2} f\|_{\infty,R_{\mathbf{j}}}$". Instead, by setting

$$\tilde{r}_{\min,\mathbf{j}}(\mathbf{s}) \geq \eta_{\mathbf{j}} := \max\left\{ H_{1,\mathbf{j}}^{\frac{1}{2(p_1+r_1+2)}},\ H_{2,\mathbf{j}}^{\frac{1}{2(p_2+r_2+2)}} \right\}$$

this guarantees that for all the scaled integrals treated with the regular rule in the governing BIEs, the quadrature convergence order is at least equal to $5/2 + \min\{p_1 + r_1, p_2 + r_2\}$. In order to have just one threshold δ for all the integrals involving the same geometry map, for the k-th patch let

$$\delta = \delta_k := \max_{\mathbf{j}\in\mathcal{I}_k} \eta_{\mathbf{j}}.$$

5. Numerical examples

In this section, the numerical scheme is tested on both interior and exterior Helmholtz problems. The boundary conditions are of either Dirichlet or Neumann type.

Two well-known benchmarks for exterior problems are the pulsating sphere and the rigid scattering on a sphere; see for instance [14–16]. It covers a plane wave scattering problem and scattering of spherical waves emitted by an acoustic point source next to a sphere, for which the exact solution is also known in series form. The sphere has radius $R = 1$ and is parameterized by 6 quartic ($\mathbf{d}_g = (4,4)$) NURBS patches, see Fig. 3(a) and refer to [37] for details. As in [38], the considered quartic NURBS parameterization based on cube topology is preferred over the 8-patch tiling in order to avoid singularities in the geometry description at the poles of the sphere. A preliminary manufactured example on unit cube is considered at the end of the section to test a simple adaptive numerical integration for nearly singular inter-patch integrals at the sharp interfaces of the geometry.

As for interior problems, a (possibly distorted) torus and a manufactured solution in its interior that is commonly used in the IgA-BEM literature are considered; see for example [14,15]. The undistorted torus has inner radius 1, outer radius 3, and is exactly represented in a 16-patch quadratic ($\mathbf{d}_g = (2,2)$) NURBS form, see Fig. 3(b) and also [12] for details. The distorted torus is obtained by changing a single outer patch as in Fig. 3(c), see Section 5.5 for more details.

The quality of the achieved numerical results is evaluated by comparing the numerical solution u_h to the exact solution u^{ex}, which is available for all tests, and measuring the on-surface relative error in the $L^2(\Gamma)$ norm:

$$e_{L^2} = \frac{\|u_h - u^{ex}\|_{L^2(\Gamma)}}{\|u^{ex}\|_{L^2(\Gamma)}}.$$

Table 3
Condition numbers of the system matrix when discontinuous or non-conforming continuous discretization spaces are used on a sphere. All patches have $n \times n$ elements, except for one patch that has $3n/2 \times 3n/2$. In all cases, $\mathbf{d} = (4,4)$ and $\kappa = 2$.

n	Dirichlet boundary conditions		Neumann boundary conditions	
	C^{-1} space	C^0 space	C^{-1} space	C^0 space
4	8.47e+01	1.40e+02	9.05e+01	1.52e+02
8	7.44e+01	1.39e+02	7.68e+01	1.50e+02
12	7.03e+01	1.39e+02	7.20e+01	1.50e+02
16	6.84e+01	1.38e+02	6.99e+01	1.50e+02

For the discretization space V, on each patch standard tensor product B-splines of bi-degrees $\mathbf{d} = (d,d)$ and of highest continuity are employed; in all experiments (except for the pulsating sphere) C^0 continuity of the basis functions across patch interfaces is enforced. Moreover, in the point source acoustic scattering problem and in the case of a distorted torus, non-conforming spaces are used to better approximate the local features of the exact solution. The non-conforming spaces are implemented as linear constraints based on knot removal, as explained in Section 3.3. The choice of knot removal over knot insertion does not affect the accuracy of any presented numerical solution, since the two approaches are algebraically equivalent and the condition number of the system matrix is not a limiting factor.

To illustrate this point with an example, consider the unit sphere of Fig. 3(a) and suppose that the CBIE (8) or (10) is discretized for $\kappa = 2$ using a multi-patch spline space of bi-degree $\mathbf{d} = (4,4)$ with $n \times n$ uniform elements on every patch, except for one patch with $3n/2 \times 3n/2$ uniform elements (the space is allowed to be discontinuous; n is a positive even integer). Table 3 reports the condition number of the system matrix as a function of n for both discontinuous and non-conforming continuous discretization spaces, and for both Dirichlet and Neumann boundary conditions (which determine the choice between (8) and (10)). As it can be seen from the results in the table, there is not much difference in the condition number between the two boundary conditions, and in all four cases the condition number remains bounded as n is increased, levelling to a constant of the order of 10^2. Moreover, the introduction of non-conforming continuity constraints only increases the constant by a factor of about 2 when compared to the discontinuous case. For completeness, a similar behaviour is also observed in the numerical experiments that make use of conforming continuous discretization spaces, like those of Section 5.2: in that case, the condition numbers converge to around 70 and 75 for Dirichlet and Neumann boundary conditions, respectively.

5.1. Pulsating sphere

The following problem serves as a benchmark test for the developed quadrature rules; it is also referred to as a patch test for IgA-BEM. The model can be used for example to numerically compute the sound pressure at a distance r from the centre of the sphere for a constant wave

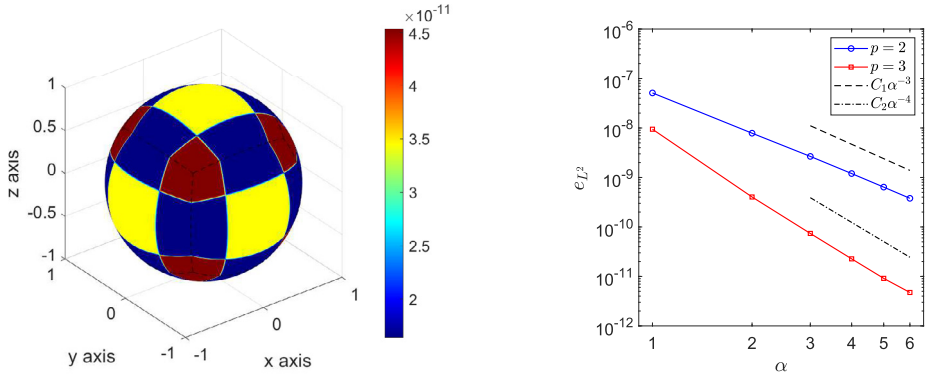

(a) On surface error distribution ($\alpha = 6, m = 2, p = 2$) (b) Error convergence plot

Fig. 4. Pulsating sphere for $\kappa = 1$.

speed in the radial direction. For the Neumann boundary conditions $u_N \equiv -e^{i\kappa}(i\kappa - 1)/(4\pi)$ for $\mathbf{x} \in \Gamma$, the analytic solution is $u = e^{i\kappa r}/(4\pi r)$, hence the missing Cauchy datum is $\phi \equiv e^{i\kappa}/(4\pi)$ for $\mathbf{x} \in \Gamma$.

Since the geometry representation of the sphere is exact and ϕ is constant over the entire boundary, the error can be attributed solely to numerical integration. On each patch the knot vectors describing the local part of the discretization space $\hat{S}^{(\ell)}_{h^{(\ell)}}$ are

$$T_1^{(\ell)} = T_2^{(\ell)} = \begin{bmatrix} 0 & 0.25 & 0.5 & 0.75 & 1 \end{bmatrix}.$$

The collocation points are midpoints of the knots, mapped to the physical domain via the geometry map. Fixing $\kappa = 1, \mathbf{d} = (0,0)$ and setting $c_u = 0.25$ in the definition of the threshold used for near singularity detection, the L^2 error of the approximate solution with respect to different number of quadrature nodes on the support of B-splines is measured. The number n_q of quadrature nodes increases in each coordinate direction with $n_q = 12\alpha + 1$, for $\alpha = 1, 2, \ldots, 6$. The same quadrature nodes are used for singular, regularized and regular integrals.

In Fig. 4(a) observe the error distribution (modulus of the difference between the exact and approximate solution) for $\alpha = 1$, $m = 2$ (number of terms in the singularity extraction), $p = 2$ (spline bi-degree (p, p) of the QI operator). The error is well evenly spread on the boundary with a slight increase around patch corners, where the kernel expansion is more critical. The error is also slightly higher in the interior of the patches than in the neighbourhood of the edges since the area of interior mapped cells is slightly larger than the boundary ones. In Fig. 4(b) observe that error convergence order is impacted by the choice of m and p. For $p = m = 2$ the obtained order of convergence is 3. If both m and p are increased to 3, the order of convergence increases to 4.

The comparison can be done with Figure 6(a) of [15], where $R\kappa = 1$ as in experiments in this work. In the referred picture the results obtained with the new approach (termed as *New*) are compared to those produced by the method introduced in [14] (termed as *Old*). The relative L^2 error, e_{L^2}, is shown against the total number of quadrature nodes n_{qp} (where the number of quadrature nodes in the elements with active singularity is not taken into account). In the current work the total number of quadrature nodes, for $\alpha = 6$, is $6 \cdot 16 \cdot 72^2 \approx 5.0 \cdot 10^5$ achieving an error (with $p = 3$) of order 10^{-11}. This is a much better result than that produced by the *Old* approach but also better than that given by the *New* one.

5.2. Rigid scattering of a plane wave on a sphere

Suppose that in a rigid scattering problem the incident acoustic pressure p_{inc} is produced by the plane wave

$$p_{\text{inc}}(\mathbf{x}) := Ae^{i\kappa(\mathbf{v}\cdot\mathbf{x})}$$

characterized by amplitude A and wave vector $\kappa\mathbf{v}$, with $\mathbf{v}$ being a unit vector prescribing the direction of the wave. This pressure wave is incident on a rigid body represented by a volume $\Omega^{(i)}$ with boundary Γ, where the rigidity assumption implies that it reacts producing in $\Omega^{(e)}$ an additional scattered pressure field p verifying the Helmholtz equation in $\Omega^{(e)}$, the Sommerfield radiation condition at infinity and having a variation in the normal direction on Γ opposite to that of p_{inc}, see for example [15]. The scattered pressure p is the unknown to be determined in $\Omega^{(e)}$ and it can be written as the difference between a total pressure field p_{tot} and p_{inc}, where p_{tot} is such that

$$\begin{cases} p_{\text{tot}}(\mathbf{x}) & = p_{\text{inc}}(\mathbf{x}) + (V_\kappa \partial_n p_{\text{tot}}) - (K_\kappa p_{\text{tot}})(\mathbf{x}), \ \mathbf{x} \in \Omega^{(e)} \\ \partial_n p_{\text{tot}}(\mathbf{x}) & = 0, \ \forall \mathbf{x} \in \Gamma. \end{cases} \tag{52}$$

Note that in this experiment Γ is assumed to be a sphere with radius $R = 1$ (again parameterized as previously described) and so, by symmetry, it can be assumed that $\mathbf{v} = (1,0,0)$ without loss of generality. The problem can be used as a benchmark because the analytic expression of p is a priori known, see for example [16],

$$p(\mathbf{x}) = -A \sum_{\nu=0}^{\infty} \frac{i^\nu (2\nu+1) j'_\nu(\kappa R)}{h'_\nu(\kappa R)} P_\nu(\cos(\theta))\, h_\nu(\kappa r), \tag{53}$$

where $\mathbf{O}$ is the centre of the sphere, $r = \|\mathbf{x} - \mathbf{O}\|_2$, θ is the angle between the vectors $\mathbf{x} - \mathbf{O}$ and $\mathbf{v}$, j_ν is the spherical Bessel function of the first kind, h_ν is the spherical Hankel function of the first kind, h'_ν and j'_ν are the derivatives of j_ν and h_ν, and P_ν is the Legendre polynomial of order ν. In the current experiments A is set to 1 and the infinite series is truncated after $\nu = 10$, which provides sufficient accuracy to study the convergence of the developed numerical scheme for the considered frequencies.

The values considered for κ in the experiments are $\kappa = 1, 2, 3$, which for usual atmospheric air correspond to frequencies of approximately $50, 100, 150$ Hz. The aim of the numerical test is to approximate the unknown Dirichlet Cauchy datum $\phi = p_{\text{tot}}|\Gamma$ (alternatively also denoted below just with u which denotes also its extension to $\Omega^{(e)}$). Thus, considering that the corresponding given Neumann datum is homogeneous, the boundary integral equation to be considered simplifies to the following one,

$$(K_\kappa + \frac{1}{2} I)\phi(\mathbf{x}) = p_{\text{inc}}(\mathbf{x}), \quad \mathbf{x} \in \Gamma. \tag{54}$$

The discretization of this BIE has been done by using a conforming globally C^0 multi-patch IgA space with uniform elements on each patch. For this experiment the following simplification is possible

$$\frac{\mathbf{r} \cdot \mathbf{n}_\mathbf{y}}{r^2} = -\frac{1}{2R},$$

where $\mathbf{n}$ points towards the centre of the sphere since the considered problems are exterior. Then, by taking into account (7), regular rules are used for the imaginary part of the double layer kernel K_κ, while, for its real part, singular rules are used for the kernel $1/r$. The constant

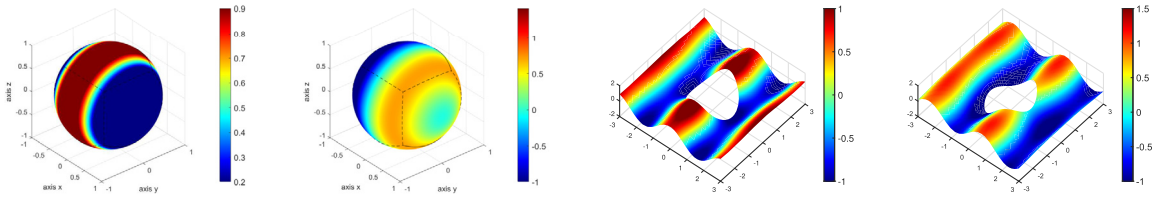

(a) The real part of the total pressure on the sphere

(b) The imaginary part of the total pressure on the sphere

(c) The real part of the total pressure on the equatorial plane

(d) The imaginary part of the total pressure on the equatorial plane

Fig. 5. Rigid scattering of a plane wave on a sphere with $\kappa = 2$: on and off surface total pressure distributions.

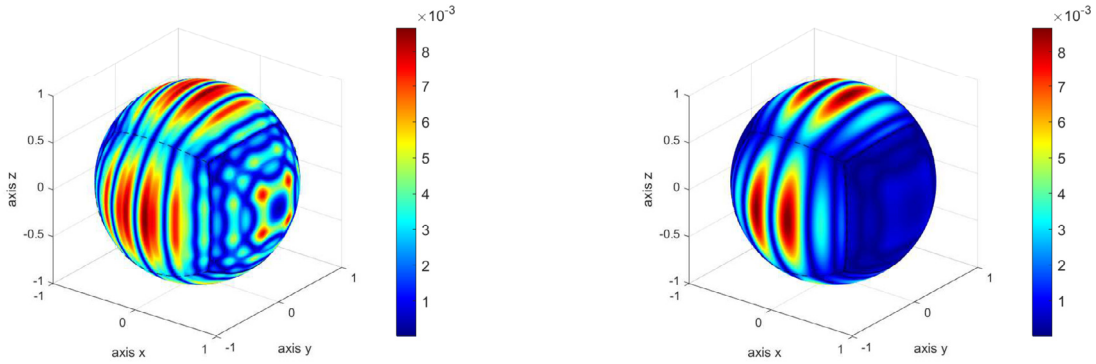

(a) On surface error distribution ($d = 2\,, n = 5$)

(b) On surface error distribution ($d = 4\,, n = 3$)

Fig. 6. Rigid scattering of a plane wave on a sphere with $\kappa = 2$: on surface distribution of the modulus of the absolute error ($N_{\mathrm{DOF}} = 218$).

c_u involved in the near singularity detection phase in this experiment is chosen to be equal to 0.1. In all the tests reported for this and also in the next experiments for all the three kinds of quadrature rules the QI degree is 2 for the singular and regularized rules and it is 4 for the regular ones. The use of a low degree is reasonable for regularized integrals, since higher degrees of the quasi interpolating spline are profitable only if the function it approximates is sufficiently regular. For singular integrals a low degree has been preferred to reduce the cost of the related weight computation. For all the involved quadrature rules, in this experiment the chosen number of QI nodes (uniformly distributed in the support of each trial B-spline function) is $7, 9, 11$, respectively for degrees $d = d_1 = d_2 = 2, 3, 4$, on both coordinate directions. Note that for any degree this corresponds to select the nodes at the knots of the trial B-spline and at their midpoints in each coordinate.

In order to underline the oscillating nature of the solution of (54) and of the related domain solution, Fig. 5 shows the real and the imaginary part of the exact Cauchy datum $\phi = p_{\mathrm{tot}}|\Gamma$ for $\kappa = 2$, (frequency of about 100 Hz) together with the corresponding real and imaginary parts of the total pressure in an area of the equatorial plane exterior to the sphere. Fig. 6 shows the distribution on the sphere of the modulus of the absolute error obtained with both the choices $d = 2$ and $d = 4$. Note that the number of degrees of freedom ($N_{\mathrm{DOF}} = 218$) is the same on the left and on the right of this figure, since the number n^2 of elements in each patch is chosen in order to ensure the fulfillment of such goal, that is $n = 5$ for $d = 2$ and $n = 3$ for $d = 4$. This means that when $d = 4$, the elements are larger than in the other case and so an analogous maximal error on the surface is acceptable. Note also that the error distribution on the sphere implies a slightly lower $L^2(\Gamma)$ relative error on surface for $d = 4$ (it is 3.20e-03 for $d = 2$ and 2.43e-03 for $d = 4$). Results in the current work can be compared with those, less accurate, shown in Figure 13 of [16], which refers to $\kappa = 2$, $R = 1$, $d = 4$ as well, and are obtained with $N_{\mathrm{DOF}} = 200$.

The off surface quality of results is reported in Fig. 7, as it is done in [14]. Focusing on the approximation of the modulus of the solution, the figure shows the results obtained on the exterior equatorial circumference C with radius 10 and for $d = 2$ (the other parameters are chosen as already described), where the reported error is the following one

$$e_P(\mathbf{x}) := \frac{|\,|u_h(\mathbf{x})| - |u^{ex}(\mathbf{x})|\,|}{|u^{ex}(\mathbf{x})|}. \tag{55}$$

The figure outlines a good conformability between the moduli of the exact and of the numerical solution obtained with very few degrees of freedom for both $\kappa = 1$ and $\kappa = 3$. The quality of exterior reconstructions can be further checked by looking at the distribution on C of the error e_P. Figs. 7(c) and 7(d) can be compared respectively with Figure 17 (where $\kappa = 2$, but $R = 0.5$) and Figure 20 (where $\kappa = 6$, but $R = 0.5$) of [14], confirming the better performance of approach in the current study. It should be remarked, however, that the accuracy of the obtained results in [14] is probably also influenced by the adopted singular parameterization of the sphere, as underlined in [15].

The analysis of the results for this experiment is completed by Fig. 8, which shows the $L^2(\Gamma)$ relative error e_{L^2} as a function of n for d ranging between 2 and 4, confirming its nice convergence behaviour for all the considered values of κ. The 6 patch parameterization of the sphere corresponds to Parameterization 2 of [15]; in particular for this example, the plot corresponding to $d = 4$ in Fig. 8(a) in current work is compared to the plot related to Parameterization 2 IGABEM CC-BIE (Conventional Collocation BIE), shown in Figure 12 of [15]. For a precise comparison note that $n = 1, 2, \ldots, 7$ in [15] in corresponds to $N_{\mathrm{DOF}} = 98, 152, 218, 296, 386, 488, 602$ in current work. Hence, the results obtained in current work show better accuracy than the approach used in [15].

5.3. Rigid scattering of spherical waves on a sphere

Suppose that in a rigid scattering problem the incident acoustic pressure p_{inc} is produced by a point source centred at $\mathbf{x}_s \in \mathbb{R}^3$, with $\|\mathbf{x}_s\|_2 > 1$:

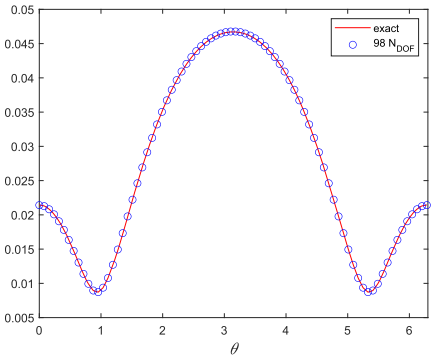

(a) Modulus of the exact and of the numerical solution on $\mathcal{C}$ for $\kappa = 1$

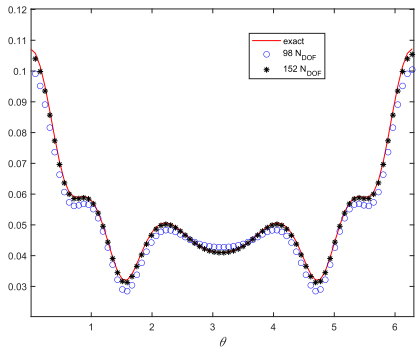

(b) Modulus of the exact and of the numerical solution on $\mathcal{C}$ for $\kappa = 3$

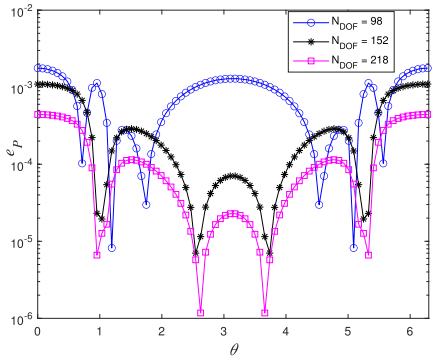

(c) Distribution of the error e_P on $\mathcal{C}$ for $\kappa = 1$

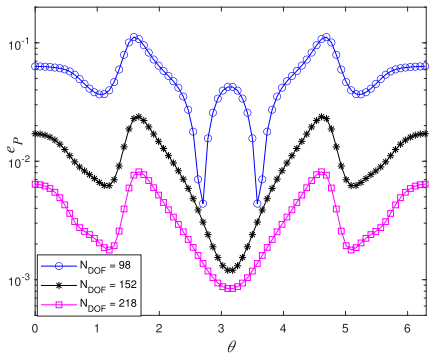

(d) Distribution of the error e_P on $\mathcal{C}$ for $\kappa = 3$

Fig. 7. Rigid scattering of a plane wave on a sphere: results on the exterior equatorial circumference $\mathcal{C}$ ($d = 2, p = 2, 2, 4$).

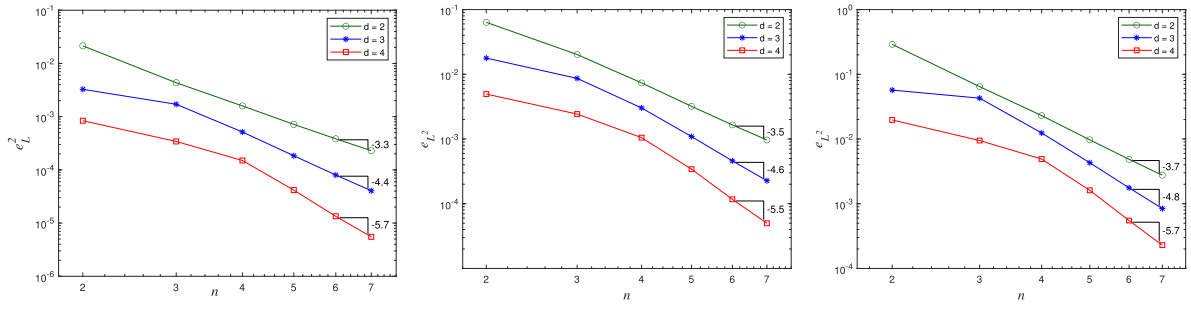

(a) $\kappa = 1$ (b) $\kappa = 2$ (c) $\kappa = 3$

Fig. 8. Rigid scattering of a plane wave on a sphere: $L^2(\Gamma)$ error e_{L^2} as a function of n, number of elements in each coordinate direction for each patch (conforming discretization).

$$p_{\text{inc}}(\mathbf{x}) = A\,\mathcal{G}_\kappa(\mathbf{x}, \mathbf{x}_s) = A\,\frac{e^{i\kappa\|\mathbf{x}-\mathbf{x}_s\|_2}}{4\pi\,\|\mathbf{x}-\mathbf{x}_s\|_2}.$$

The variable A denotes the amplitude of the emitted wave. The singularity of p_{inc} at $\mathbf{x}_s$ is not an issue, because it can be proven that the regularity assumptions $p_{\text{inc}} \in L^1_{\text{loc}}(\mathbb{R}^3)$ and $p_{\text{inc}} \in C^\infty(U)$ with U neighbourhood of Γ are sufficient to establish the well-posedness of the rigid scattering problem (52), see [39].

Like in the previous subsection, an exact analytic expression for the scattered pressure p on the surface of a sphere with radius $R = 1$ can be found by a series expansion in terms of Hankel's functions of the first kind [40]:

$$p(\mathbf{x}) = -A\sum_{\nu=0}^{\infty} i\kappa\, h_\nu(\kappa\,\|\mathbf{x}_s\|_2)\,\frac{(2\nu+1)j'_\nu(\kappa R)}{4\pi h'_\nu(\kappa R)}\,P_\nu(\cos(\theta))h_\nu(\kappa r). \tag{56}$$

By the sphere's symmetry, $\mathbf{x}_s = (x_s, 0, 0)$ without loss of generality. If the acoustic source is close to the surface of the sphere, that is, x_s is only slightly larger than 1, then the modulus of the total pressure will decay very rapidly on the surface of the sphere away from the point $(1, 0, 0) \in \Gamma$.

Therefore, smaller numerical errors are expected if the discretization space V is finer on the patch containing that point, and so for this test the non-conforming spaces introduced in Section 3.3 is used. In these numerical experiments A is set to 1, and the infinite series (56) is truncated after $\nu = 50$, because its convergence rate is slower than (53), especially for acoustic sources near the surface of the sphere. Once again, the simplified boundary integral equation (54) is considered, because the Neumann datum is homogeneous. All the details regarding quadrature rules and near singular detection are the same as for the plane wave tests.

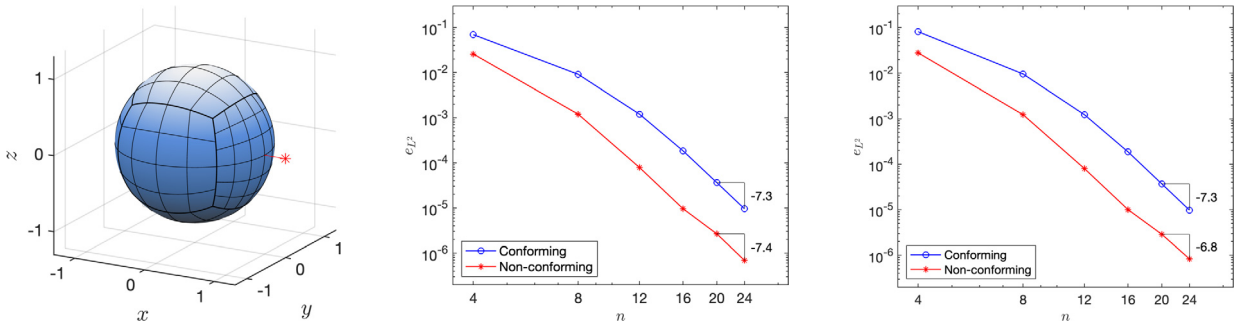

(a) Non-conforming spaces, $n = 4$ (b) $\kappa = 2$ (c) $\kappa = 3$

Fig. 9. Rigid scattering of spherical waves on a sphere. On the left: discretization elements in the $n = 4$ non-conforming case. The acoustic source is marked with a red asterisk. On the right: $L^2(\Gamma)$ error e_{L^2} as a function of n for $d = 4$ and $\kappa = 2, 3$. In the conforming case, every patch has $n \times n$ uniform elements. In the non-conforming case, the patch in front of the acoustic source has $3n/2 \times 3n/2$ uniform elements.

The two plots in Fig. 9 show a comparison of the numerical errors between conforming and non-conforming discretization spaces for $d = 4$ in the spline bi-degree $\mathbf{d} = (d, d)$, $x_s = 1.3$ and $\kappa = 2, 3$. In the conforming case, the BIE is discretized using a globally C^0 multi-patch IgA space with the same number $n \times n$ of uniform elements on every patch. In the non-conforming case, everything is the same except for the patch that contains the point $(1, 0, 0)$, on which the number of uniform elements is $3n/2 \times 3n/2$. This refinement increases the total number of degrees of freedom N_{DOF} by a modest amount, approximately 25%, and this relative increase is asymptotically independent of n. The numerical results show how the increase in N_{DOF} is largely outweighed by the consequent reduction of global error in the $L^2(\Gamma)$ norm by an order of magnitude. Hence, even when taking into account the additional calculations required for the assembly of the constraints (25) or (27) in the non-conforming case, the choice of non-conforming spaces provides an overall significant reduction of the numerical error for a given total computational budget.

5.4. Acoustic problem interior to a torus

This example is taken from [14]. The Helmholtz equation is considered with exact acoustic potential chosen to be

$$\phi(\mathbf{x}) = \sin(\kappa x/\sqrt{3}) \sin(\kappa y/\sqrt{3}) \sin(\kappa z/\sqrt{3}). \tag{57}$$

The Neumann datum is prescribed by computing the acoustic velocity field as $(\partial\phi/\partial\mathbf{n})(\mathbf{x})$ for $\mathbf{x} \in \Gamma$, where $\mathbf{n}$ denotes the outward unit normal vector to the surface. In the numerical experiment, the wavenumber κ is set to 2, and a conforming globally C^0 discretization space with spline bi-degree (d, d) for $d = 2, 3$ is considered. The constant c_u used in (30) for near singularity detection is set to 0.1. Regarding the adopted quadrature scheme, QI degree 4 is used for regular integrals, and degree 2 is used for singular and regularized integrands. For $d = 2$, the number m of terms in the singularity extraction is set to 2, and the number of uniformly spaced quadrature nodes in each parametric direction on the support of a B-spline is set to 7; hence nodes are just knots and knot midpoints of B-splines. When $d = m = 3$, 9 quadrature nodes are used for singular and regular integrals, and 13 nodes are used for regularized integrals.

The parametric coordinates on every patch are oriented so that the first coordinate runs along the toroidal direction (the one related to the outer radius) and the second coordinate runs along the poloidal direction (the one related to the inner radius). Since the ratio between outer radius and inner radius is 3, uniform knot vectors with $h_1^{(\ell)} = h_2^{(\ell)}/3$ are used on every patch $\Gamma^{(\ell)}$ for all tests, so that the supports of the B-splines $B_{\mathbf{j},\mathbf{d}}^{\mathbf{T}^{(\ell)}}$ in physical space are approximately squares. This choice maximizes the approximation power of the spline space for a given number of basis elements.

Although the imaginary part of the acoustic potential ϕ is zero on the entire boundary Γ, the chosen wavenumber produces several oscillations in the real part of ϕ, see Fig. 10(a). The error e_{L^2} is plotted with respect to the refinement parameter h_1 in Fig. 10(b); a convergence rate equal to $d + 1$ can be observed.

5.5. Acoustic problem interior to a distorted torus

This problem is also an interior problem with acoustic potential (57), but this time the boundary datum is of Dirichlet type and the toroidal geometry is distorted on one outer patch. To better approximate the solution $\partial\phi/\partial\mathbf{n}$ on the distorted patch $\Gamma^{(k)}$, non-conforming globally C^0 spaces are used for the discretization, so that $h_1^{(k)}$ may be smaller than $h_1^{(\ell)}$ for $\ell = 1, \dots, M$ with $k \neq \ell$. As before, $h_2^{(\ell)} = 3h_1^{(\ell)}$ on every patch.

The distorted patch $\Gamma^{(k)}$ is a quadratic NURBS surface defined as follows. First, the 3×3 control net of the undistorted patch is uniformly refined by knot insertion so that its size becomes 13 in the first parametric direction and 9 in the second. Then, only the innermost 7×3 subset of control points is changed, to ensure a C^2 connection of patch $\Gamma^{(k)}$ to neighbouring patches. The points in this subset are moved along the direction normal to the surface by

$$\begin{matrix} -1/16 & -1/8 & 0 & 1/8 & 0 & -1/8 & -1/16 \\ -1/8 & -1/4 & 0 & 1/4 & 0 & -1/4 & -1/8 \\ -1/16 & -1/8 & 0 & 1/8 & 0 & -1/8 & -1/16 \end{matrix}$$

respectively, so that three bumps are formed (two inward and one outward), as shown in Fig. 3(c).

For the numerical tests, parameters $\kappa = 2$ and spline bi-degree $(2, 2)$ were chosen. All the details regarding quadrature rules and near-singular detection are the same as for the previous test with no distortion. Fig. 11(a) compares the global L^2 error between conforming and non-conforming discretizations as $h_1^{(\ell)} \to 0$. Aiming for a total increase in N_{DOF} of around 15%, the value of h_1 on the distorted patch is halved compared to h_1 on the other patches (the relative increase in N_{DOF} is asymptotically independent of h_1). In this test, the use of nonconforming spaces reduces e_{L^2} by a factor of around 2, a less drastic reduction compared to the rigid scattering test, but still significant, given the modest increase in computational cost (proportional to N_{DOF}). Figs. 11(b) and 11(c) show the on surface modulus of the numerical error for $h_1^{(\ell)} = 1/9$ on the undistorted patches and either $h_1^{(k)} = 1/9$ or $h_1^{(k)} = 1/18$ on the distorted patch (the conforming and hierarchically non-conforming cases, respectively). It is apparent how even a small local increase in the total number of degrees of freedom (around 12%) is enough to more than halve the error in the $L^\infty(\Gamma)$ norm.

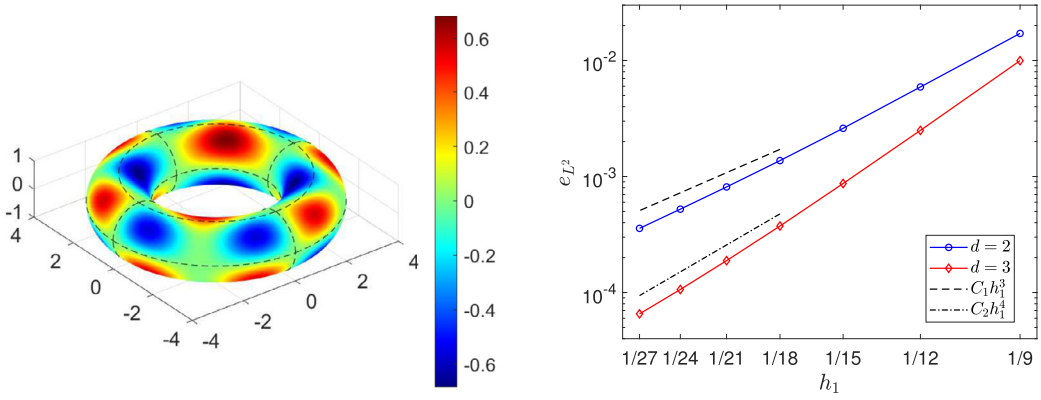

(a) On surface acoustic potential

(b) Error convergence against element size h_1

Fig. 10. Interior acoustic problem, undistorted torus, $\kappa = 2$.

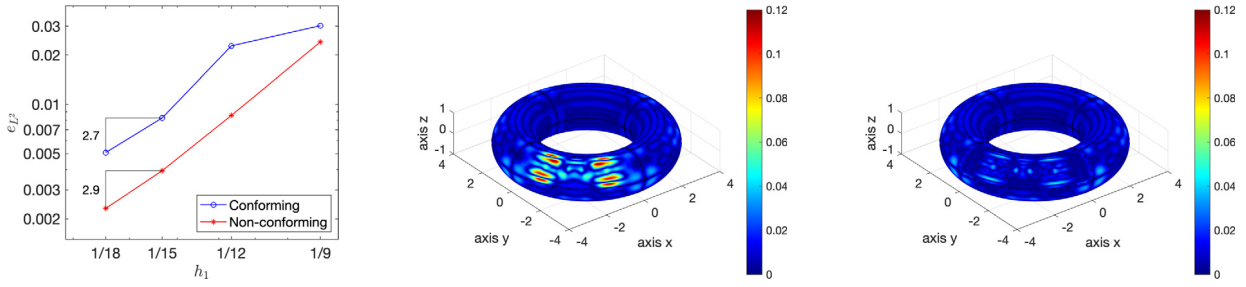

(a) Error convergence against h_1, element size on the undistorted patches

(b) On surface modulus of the numerical error, conforming spaces, $h_1 = 1/9$, $h_1^{(k)} = 1/9$, $N_{\mathrm{DOF}} = 880$

(c) On surface modulus of the numerical error, non-conforming spaces, $h_1 = 1/9$, $h_1^{(k)} = 1/18$, $N_{\mathrm{DOF}} = 985$

Fig. 11. Interior acoustic problem, distorted torus, $\kappa = 2$ and $d = 2$.

5.6. A manufactured example on a cuboidal geometry

The last example is a preliminary experiment on a non-smooth geometry – a manufactured exterior boundary problem on a geometry with sharp corners to test a simple adaptive quadrature procedure. For the Neumann boundary conditions set to $u_{\mathrm{N}}(\mathbf{x}) = e^{i\kappa r}(i\kappa r - 1)(\mathbf{x}\cdot\mathbf{n})/(4\pi r^3)$ for $\mathbf{x} \in \Gamma$, $r = \|\mathbf{x}\|_2$ and $\mathbf{n}$ inward normal unit vector, the missing Cauchy datum is equal to $\phi(\mathbf{x}) = e^{i\kappa r}/(4\pi r)$ for $\mathbf{x} \in \Gamma$.

Due to sharp corners in the geometry and proportionally larger solid angles inside Ω, the function c in (5) is not everywhere equal to $1/2$; if the source point lies inside the cuboid edge or at the vertex, then the value of c is equal to $3/4, 7/8$, respectively. Reduced smoothness of the geometry can greatly impact the accuracy of the procedure for inter-patch nearly singular integration, described in Section 4.5. In such case it is preferable to replace the routine with a rule for regular integrals (explained in Section 4.3) with higher density of quadrature nodes nearer the source point. Such idea is pursuit in this test, where for simplicity by assuming the integration domain to be given by $\{\tilde{\mathbf{F}}^{(\ell)}(\mathbf{t}) : \mathbf{t} \in [0,1]^2\}$ and the source point $\tilde{\mathbf{F}}^{(k)}(\mathbf{s})$ to lie close to $\tilde{\mathbf{F}}^{(\ell)}((0,0))$ in t_1 direction, the geometric distribution of n_q quadrature nodes in direction t_1 is then given as

$$\left\{ \frac{0}{n_q-1}\omega^{n_q-1}, \quad \frac{1}{n_q-1}\omega^{n_q-2}, \quad \frac{2}{n_q-1}\omega^{n_q-3}, \quad \ldots, \quad \frac{n_q-2}{n_q-1}\omega^{1}, \quad \frac{n_q-1}{n_q-1}\omega^{0} \right\}. \tag{58}$$

The common ratio $\omega < 1$ is set so that the quotient between the leftmost and the rightmost cell sizes in (58) is equal to quotient $\|\tilde{\mathbf{F}}^{(k)}(\mathbf{s}) - \tilde{\mathbf{F}}^{(\ell)}((0,0))\|_2 / \|\tilde{\mathbf{F}}^{(k)}(\mathbf{s}) - \tilde{\mathbf{F}}^{(\ell)}((1,0))\|_2$.

The boundary of the unit cube is represented as a 6-patch linear B-spline geometry. For the numerical tests let $\kappa = 1, 2, 5$, $\mathbf{d} = (2,2)$, $c_u = 0.25$ and the number n_q of quadrature nodes is fixed to 7 in each coordinate direction on the support of B-spline trial functions for regular and singular integrals. The number of nodes needs to be increased to 13 for the adaptive integration for the inter-patch nearly singular integrals. As before, the bi-degree $\mathbf{p}$ of the QI operator is set to $(4,4)$ for the regular integrals and to $(2,2)$ otherwise.

The numerical solutions are tested against the exact solution with respect to mesh size $h = h^{(\ell)} = 1/4, 1/5, \ldots, 1/12$, $\ell = 1, 2, \ldots, 6$; the results are shown in Fig. 12(b). For all tested κ the optimal order of convergence h^3 is achieved. The error distribution for $\kappa = 1$ and $h = 1/7$ is depicted Fig. 12(a), it is relatively well spread on the boundary across every patch.

6. Conclusion

In this paper 3D Helmholtz problems are addressed using isogeometric BEMs on smooth geometries with a general multi-patch parametric NURBS representation, relying for the discretization on conforming and also non-conforming multi-patch C^0 spline spaces, since derivation and integration is easier for splines compared to NURBS without any loss in approximation power. The governing boundary integral equations are numerically approximated by a collocation scheme. The adopted quadrature rules for both regular and singular integrals are tailored for B-splines and they allow a profitable function-by-function matrix assembly. A procedure is proposed for the automatic detection of nearly singular integrals. Besides studying the approximation power of the considered rules, an arrangement with a singularity extraction technique is proposed, extending it to the multi-patch setting for the first time. Numerical results confirm the effectiveness of the method by achieving sufficient accuracy of the numerical solution with a small number of uniformly distributed quadrature nodes.

A possible future work could be devoted to tuning the proposed methodology in both conforming and non-conforming multi-patch C^0 spline spaces for more general types of contacts between patches, a

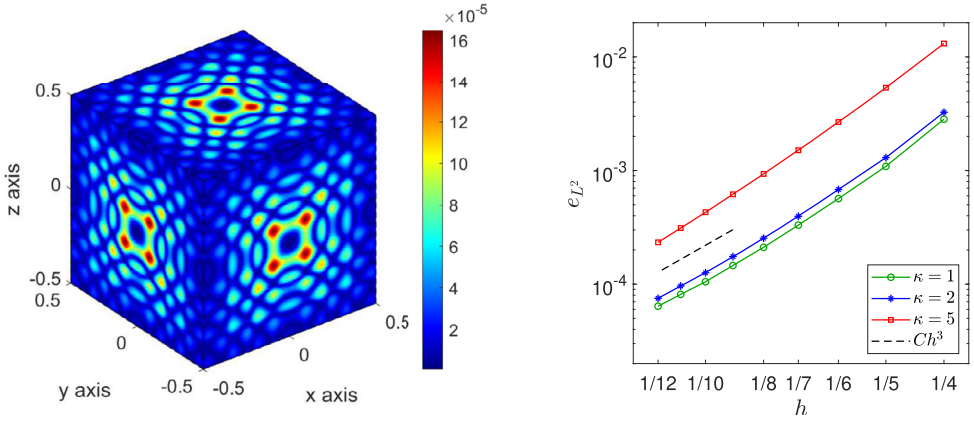

(a) On surface absolute error plot for $h = 1/7$ and $\kappa = 1$ (b) Error convergence against element size h

Fig. 12. A manufactured example on a cuboidal geometry.

preliminary experiment being the presented Helmholtz manufactured test problem formulated on the cuboidal geometry.

Data availability

Data will be made available on request.

Acknowledgements

The authors would like to express their gratitude to the reviewers for their valuable comments, which contributed to enhancing the overall quality of the manuscript. Tadej Kanduč was partially funded for developing this research by SIMAI-ACRI, which is gratefully acknowledged. The research of Antonella Falini was founded by PON Ricerca e Innovazione 2014-202 FSE REACT-EU, Azione IV.4 "Dottorati e contratti di ricerca su tematiche dell'innovazione" CUP H95F21001230006. Alessandra Sestini acknowledges the contribution of the National Recovery and Resilience Plan, Mission 4 Component 2 – Investment 1.4 - NATIONAL CENTER FOR HPC, BIG DATA AND QUANTUM COMPUTING – funded by the European Union – NextGenerationEU – (CUP B83C22002830001). The Italian authors are members of the INdAM Research group GNCS. The INdAM support through GNCS (CUP E55F22000270001) is gratefully acknowledged.

Appendix A

To provide a self-contained analysis of the developed integration procedures, a more technical part related to the behaviour of the considered singular kernels is given in this appendix.

Let Γ be a regular surface admitting a C^2 regular parameterization on $D := [0,1]^2$, $\mathbf{F} : D \to \Gamma$, $\mathbf{t} = (t_1, t_2) \mapsto \mathbf{F}(\mathbf{t})$. Furthermore, for any fixed $\mathbf{s} \in D$, let us introduce the following notation,

$$\mathbf{r}_\mathbf{s}(\mathbf{t}) := \mathbf{F}(\mathbf{t}) - \mathbf{F}(\mathbf{s}),\ r_\mathbf{s}(\mathbf{t}) := \|\mathbf{r}_\mathbf{s}(\mathbf{t})\|_2,\ \boldsymbol{\nu}(\mathbf{t}) := \frac{\partial \mathbf{F}}{\partial t_1}(\mathbf{t}) \times \frac{\partial \mathbf{F}}{\partial t_2}(\mathbf{t}).$$

Proposition 2. *For each fixed $\mathbf{s} \in D$ and for any unit vector $\mathbf{u} = (\cos\theta, \sin\theta)$ such that $\mathbf{s} + \rho\mathbf{u}$ is included in D for ρ positive and sufficiently small, it is*

$$\lim_{\rho\to 0^+} \frac{\rho}{r_\mathbf{s}(\mathbf{s}+\rho\mathbf{u})} = \frac{1}{\sqrt{E\cos^2\theta + 2F\sin\theta\cos\theta + G\sin^2\theta}}, \tag{59}$$

$$\lim_{\rho\to 0^+} \frac{\mathbf{r}_\mathbf{s}(\mathbf{s}+\rho\mathbf{u})\cdot\boldsymbol{\nu}(\mathbf{s}+\rho\mathbf{u})}{r^2(\mathbf{s}+\rho\mathbf{u})} = -\frac{1}{2}\frac{L\cos^2\theta + 2M\sin\theta\cos\theta + N\sin^2\theta}{E\cos^2\theta + 2F\sin\theta\cos\theta + G\sin^2\theta}, \tag{60}$$

which are both finite limits, with E, F, G and L, M, N respectively denoting the coefficients of the first and second fundamental forms (with respect to the non-normalized normal $\boldsymbol{\nu}$) of $\mathbf{F}$ evaluated at $\mathbf{s}$,

$$\begin{aligned} E &:= \frac{\partial \mathbf{F}}{\partial t_1}(\mathbf{s})\cdot\frac{\partial \mathbf{F}}{\partial t_1}(\mathbf{s}), \quad F := \frac{\partial \mathbf{F}}{\partial t_1}(\mathbf{s})\cdot\frac{\partial \mathbf{F}}{\partial t_2}(\mathbf{s}), \quad G := \frac{\partial \mathbf{F}}{\partial t_2}(\mathbf{s})\cdot\frac{\partial \mathbf{F}}{\partial t_2}(\mathbf{s}), \\ L &:= \boldsymbol{\nu}(\mathbf{s})\cdot\frac{\partial^2 \mathbf{F}}{\partial t_1^2}(\mathbf{s}), \quad M := \boldsymbol{\nu}(\mathbf{s})\cdot\frac{\partial^2 \mathbf{F}}{\partial t_1 \partial t_2}(\mathbf{s}), \quad N := \boldsymbol{\nu}(\mathbf{s})\cdot\frac{\partial^2 \mathbf{F}}{\partial t_2^2}(\mathbf{s}). \end{aligned} \tag{61}$$

Proof. Setting for brevity $\mathbf{F}_i := \frac{\partial \mathbf{F}}{\partial t_i}(\mathbf{s})$, $i = 1,2$ and $\mathbf{F}_{i,j} := \frac{\partial^2 \mathbf{F}}{\partial t_i \partial t_j}(\mathbf{s})$, $i,j = 1,2$, and using the short notation $\mathbf{r} = \mathbf{r}(\mathbf{s}+\rho\mathbf{u}), r = r(\mathbf{s}+\rho\mathbf{u}), \boldsymbol{\nu} = \boldsymbol{\nu}(\mathbf{s}+\rho\mathbf{u})$, let

$$\begin{aligned} \mathbf{r} &= \rho(\mathbf{F}_1\cos\theta + \mathbf{F}_2\sin\theta) + \rho^2\left(\frac{1}{2}\mathbf{F}_{1,1}\cos^2\theta + \mathbf{F}_{1,2}\cos\theta\sin\theta + \frac{1}{2}\mathbf{F}_{2,2}\sin^2\theta\right) \\ &\quad + O(\rho^3) \end{aligned}$$

and

$$\begin{aligned} \boldsymbol{\nu} &= [\mathbf{F}_1 + \rho(\mathbf{F}_{1,1}\cos\theta + \mathbf{F}_{1,2}\sin\theta) + O(\rho^2)] \\ &\quad \times [\mathbf{F}_2 + \rho(\mathbf{F}_{1,2}\cos\theta + \mathbf{F}_{2,2}\sin\theta) + O(\rho^2)] \\ &= (\mathbf{F}_1 \times \mathbf{F}_2) + \rho[(\mathbf{F}_1 \times \mathbf{F}_{1,2} - \mathbf{F}_2 \\ &\quad \times \mathbf{F}_{1,1})\cos\theta + (\mathbf{F}_1 \times \mathbf{F}_{2,2} - \mathbf{F}_2 \times \mathbf{F}_{1,2})\sin\theta] + O(\rho^2). \end{aligned}$$

Since $r^2 = \rho^2(E\cos^2\theta + 2F\sin\theta\cos\theta + G\sin^2\theta) + O(\rho^3)$, it follows

$$\frac{\rho}{r} = \frac{1}{\sqrt{E\cos^2\theta + 2F\sin\theta\cos\theta + G\sin^2\theta + O(\rho)}},$$

$$\mathbf{r}\cdot\boldsymbol{\nu} = -\frac{1}{2}\rho^2\left(L\cos^2\theta + 2M\sin\theta\cos\theta + N\sin^2\theta\right) + O(\rho^3).$$

In order to confirm that the two limits in (59) and (60) are always finite, observe that their denominator can be respectively written as $\sqrt{\mathbf{u}^T M_\mathbf{s}\mathbf{u}}$ and $\mathbf{u}^T M_\mathbf{s}\mathbf{u}$, with $M_\mathbf{s}$ denoting the following symmetric 2×2 positive definite matrix associated to the first fundamental form of $\mathbf{F}$ evaluated in $\mathbf{s}$,

$$M_\mathbf{s} := \begin{pmatrix} E & F \\ F & G \end{pmatrix}. \tag{62}$$

The proof is complete. □

Note that the previous result implies that both the functions $\mathbf{t} \to \|\mathbf{t}-\mathbf{s}\|_2/r_\mathbf{s}(\mathbf{t})$ and $\mathbf{t} \to (\mathbf{r}_\mathbf{s}(\mathbf{t})\cdot\boldsymbol{\nu}(\mathbf{t}))/r_\mathbf{s}(\mathbf{t})^2$ are discontinuous at $\mathbf{t} = \mathbf{s}$. Despite this, the following corollary allows one to verify their uniform boundedness in D.

Corollary 1. *Under the assumptions of the previous proposition, both the functions $g_{1,\mathbf{s}}(\mathbf{t}) := \|\mathbf{t}-\mathbf{s}\|_2/r_\mathbf{s}(\mathbf{t})$ and $g_{2,\mathbf{s}}(\mathbf{t}) := (\mathbf{r}_\mathbf{s}(\mathbf{t})\cdot\boldsymbol{\nu}(\mathbf{t}))/r_\mathbf{s}^2(\mathbf{t})$ are bounded in their domain $D\setminus\{\mathbf{s}\}$, uniformly with respect to $\mathbf{s} \in D$.*

Proof. Since the proof is analogous for $g_{1,\mathbf{s}}$ and $g_{2,\mathbf{s}}$, let us refer only to $g_{1,\mathbf{s}}$.

Using proof by contradiction, let us assume that there exists a convergent sequence $\{(\mathbf{s}_{k_1}, \mathbf{t}_{k_1})\}$ in D^2 such that $g_{1,\mathbf{s}_{k_1}}(\mathbf{t}_{k_1}) \to +\infty$. Then, considering that $\mathbf{F}$ is continuous and injective, it holds $\rho_{k_1} := \|\mathbf{t}_{k_1} - \mathbf{s}_{k_1}\|_2 \to 0$ and the limit of the convergent sequence is equal to $(\mathbf{s}, \mathbf{s})$ for some $\mathbf{s} \in D$. Now, setting $\mathbf{t}_{k_1} = \mathbf{s}_{k_1} + \rho_{k_1}(\cos\theta_{k_1}, \sin\theta_{k_1})$, and by considering that θ_{k_1} varies in the periodic interval $[0, 2\pi]$, there exists a subsequence $\{(\mathbf{s}_{k_2}, \mathbf{t}_{k_2})\}$ of $\{(\mathbf{s}_{k_1}, \mathbf{t}_{k_1})\}$ such that $\{\theta_{k_2}\}$ tends to a certain angle θ. Then, using arguments analogous to the ones used in the proof of the previous proposition, it can be proven that

$$\lim_{k_2 \to \infty} g_{1,\mathbf{s}_{k_2}}(\mathbf{t}_{k_2}) = \frac{1}{\sqrt{E\cos^2\theta + 2F\sin\theta\cos\theta + G\sin^2\theta}}, \tag{63}$$

where E, F, G are defined in (61).

Since the limit in (63) exists, a contradiction follows, since $g_{1,\mathbf{s}_{k_3}}(\mathbf{t}_{k_3}) \to +\infty$ for every subsequence $\{(\mathbf{s}_{k_3}, \mathbf{t}_{k_3})\}$ of sequence $\{(\mathbf{s}_{k_1}, \mathbf{t}_{k_1})\}$. Since $\mathbf{F}$ is regular, all E, F, G can be bounded for all $\mathbf{s} \in D$ to obtain a common upper bound for the limit (63) for all $\mathbf{s} \in D$. □

The following last proposition is useful to estimate an upper bound for the quadrature rules for singular integrals.

Proposition 3. *Let $R \subset D$ be a rectangular integration domain with edges of dimensions H_1 and H_2. Then there exists a constant C such that for each $\mathbf{s} \in R$ it is*

$$\int_R |U(\mathbf{s}, \mathbf{t})| d\mathbf{t} \le C \max\{H_1, H_2\}, \tag{64}$$

where U is one of the two kernels U_{SL} and U_{DL} defined in (29).

Proof. By setting $\rho_{\mathbf{s}}(\mathbf{t}) := \|\mathbf{t} - \mathbf{s}\|_2$, observe that $U_{\mathrm{SL}}(\mathbf{s}, \mathbf{t}) = g_{1,\mathbf{s}}(\mathbf{t})/\rho_{\mathbf{s}}(\mathbf{t})$ and $U_{\mathrm{DL}}(\mathbf{s}, \mathbf{t}) = g_{1,\mathbf{s}}(\mathbf{t}) g_{2,\mathbf{s}}(\mathbf{t})/\rho_{\mathbf{s}}(\mathbf{t})$, where $g_{1,\mathbf{s}}$ and $g_{2,\mathbf{s}}$ are the two functions defined in the previous corollary. Thus, from the corollary itself it follows that for both the considered definitions of U, there exists a positive constant Q such that

$$|U(\mathbf{s}, \mathbf{t})| \le Q/\rho_{\mathbf{s}}(\mathbf{t}), \ \forall (\mathbf{s}, \mathbf{t}) \in D^2, \ \mathbf{s} \ne \mathbf{t}.$$

Then, denoting with $\mathcal{A}_{\mathbf{s}}$ the circle centred at $\mathbf{s}$ with radius $\sqrt{2}\max\{H_1, H_2\}$, it follows $R \subset D \cap A_{\mathbf{s}}$ and

$$\int_R |U(\mathbf{s}, \mathbf{t})| d\mathbf{t} \le \int_{D \cap \mathcal{A}_{\mathbf{s}}} |U(\mathbf{s}, \mathbf{t})| d\mathbf{t} \le Q \int_{\mathcal{A}_{\mathbf{s}}} \frac{1}{\rho_{\mathbf{s}}(\mathbf{t})} d\mathbf{t}.$$

Thus, switching to polar coordinates centred at $\mathbf{s}$ completes the proof. □

The constant C in (64) depends on $\mathbf{F}$. By prescribing common bounds for coefficients in (61) for all "well-behaved" functions $\mathbf{F}$ considered in practical applications, a common constant C can be sufficiently well estimated.

Appendix B

Proof of Proposition 1. Let $\mathcal{V}$ be the set of vertices of the patches that cover Γ, and for any $v \in \mathcal{V}$ let $\deg(v)$ be the degree of v, i.e., the number of incident edges or, equivalently, faces. By construction, the number of rows of matrix A_{coll} is

$$|\mathcal{V}| + \sum_{C_{k,\ell}} \left(\left| G_{k,\ell}(T_i^{(k)} \cap T_j^{(\ell)}, d) \right| - 2 \right) + \sum_{k=1}^{M} \left(\left| \hat{G}(T_1^{(k)}, d) \right| - 2 \right) \times \left(\left| \hat{G}(T_2^{(k)}, d) \right| - 2 \right), \tag{65}$$

obtained by counting collocation points on vertices, then those internal to edges, and finally those internal to patches, respectively. As for the non-conforming continuity constraints, their number is

$$\begin{aligned} &\sum_{v \in \mathcal{V}} (\deg(v) - 1) + \sum_{C_{k,\ell}} \#_{\mathrm{rows}}(\mathbf{K}_{k,\ell}) + \sum_{C_{k,\ell}} \#_{\mathrm{rows}}(\mathbf{C}_{k,\ell}) + \sum_{C_{k,\ell}} \#_{\mathrm{rows}}(\mathbf{K}_{\ell,k}) \\ &= \sum_{v \in \mathcal{V}} \deg(v) - |\mathcal{V}| + \sum_{C_{k,\ell}} \left| T_i^{(k)} \setminus T_j^{(\ell)} \right| + \sum_{C_{k,\ell}} \left(\left| G_{k,\ell}(T_i^{(k)} \cap T_j^{(\ell)}, d) \right| - 2 \right) \\ &\quad + \sum_{C_{k,\ell}} \left| T_j^{(\ell)} \setminus T_i^{(k)} \right|. \end{aligned} \tag{66}$$

The same number can also be obtained by the approach based on virtual knot insertion, because of identity (26). Summing (65) and (66), the total number of rows of A is

$$\begin{aligned} \#_{\mathrm{rows}}(A) &= \sum_{v \in \mathcal{V}} \deg(v) + 2 \sum_{C_{k,\ell}} \left(\left| G_{k,\ell}(T_i^{(k)} \cap T_j^{(\ell)}, d) \right| - 2 \right) \\ &\quad + \sum_{k=1}^{M} \left(\left| \hat{G}(T_1^{(k)}, d) \right| - 2 \right) \left(\left| \hat{G}(T_2^{(k)}, d) \right| - 2 \right) \\ &\quad + \sum_{C_{k,\ell}} \left| T_i^{(k)} \setminus T_j^{(\ell)} \right| + \sum_{C_{k,\ell}} \left| T_j^{(\ell)} \setminus T_i^{(k)} \right| \\ &= \sum_{v \in \mathcal{V}} \deg(v) + \sum_{k=1}^{M} \left| \hat{G}(T_1^{(k)}, d) \right| \left| \hat{G}(T_2^{(k)}, d) \right| \\ &\quad - 2 \sum_{k=1}^{M} \left| \hat{G}(T_1^{(k)}, d) \right| - 2 \sum_{k=1}^{M} \left| \hat{G}(T_2^{(k)}, d) \right| + 4M \\ &\quad + 2 \sum_{C_{k,\ell}} \left(\left| G_{k,\ell}(T_i^{(k)} \cap T_j^{(\ell)}, d) \right| - 2 \right) + \sum_{C_{k,\ell}} \left| T_i^{(k)} \setminus T_j^{(\ell)} \right| \\ &\quad + \sum_{C_{k,\ell}} \left| T_j^{(\ell)} \setminus T_i^{(k)} \right| \\ &= \sum_{v \in \mathcal{V}} \deg(v) + \#_{\mathrm{cols}}(A) - 2 \sum_{k=1}^{M} \left| \hat{G}(T_1^{(k)}, d) \right| \\ &\quad - 2 \sum_{k=1}^{M} \left| \hat{G}(T_2^{(k)}, d) \right| + 4M - \sum_{C_{k,\ell}} 4 \\ &\quad + 2 \sum_{C_{k,\ell}} \left| G_{k,\ell}(T_i^{(k)} \cap T_j^{(\ell)}, d) \right| + \sum_{C_{k,\ell}} \left| T_i^{(k)} \setminus T_j^{(\ell)} \right| + \sum_{C_{k,\ell}} \left| T_j^{(\ell)} \setminus T_i^{(k)} \right| \\ &= \sum_{v \in \mathcal{V}} \deg(v) + \#_{\mathrm{cols}}(A) - 2 \sum_{k=1}^{M} \left(\left| T_1^{(k)} \right| - d - 1 \right) \\ &\quad - 2 \sum_{k=1}^{M} \left(\left| T_2^{(k)} \right| - d - 1 \right) + 4M - \sum_{C_{k,\ell}} 4 \\ &\quad + 2 \sum_{C_{k,\ell}} \left(\left| T_i^{(k)} \cap T_j^{(\ell)} \right| - d - 1 \right) + \sum_{C_{k,\ell}} \left| T_i^{(k)} \setminus T_j^{(\ell)} \right| \\ &\quad + \sum_{C_{k,\ell}} \left| T_j^{(\ell)} \setminus T_i^{(k)} \right| \\ &= \sum_{v \in \mathcal{V}} \deg(v) + \#_{\mathrm{cols}}(A) - 2 \sum_{k=1}^{M} \left(\left| T_1^{(k)} \right| - d - 1 \right) \\ &\quad - 2 \sum_{k=1}^{M} \left(\left| T_2^{(k)} \right| - d - 1 \right) + 4M - \sum_{C_{k,\ell}} 4 \\ &\quad + \sum_{C_{k,\ell}} \left(\left| T_i^{(k)} \right| - d - 1 \right) + \sum_{C_{k,\ell}} \left(\left| T_j^{(\ell)} \right| - d - 1 \right). \end{aligned} \tag{67}$$

Since every patch has exactly 4 vertices, and every edge is shared by exactly 2 patches,

$$\sum_{v \in \mathcal{V}} \deg(v) = 4M, \qquad \sum_{C_{k,\ell}} 1 = 2M, \qquad \sum_{v \in \mathcal{V}} \deg(v) + 4M - \sum_{C_{k,\ell}} 4 = 0.$$

Moreover, by considering two different ways to count the same knot vectors (iteration over edges or over faces),

$$\sum_{C_{k,\ell}} \left(\left| T_i^{(k)} \right| - d - 1 \right) + \sum_{C_{k,\ell}} \left(\left| T_j^{(\ell)} \right| - d - 1 \right) = 2 \sum_{k=1}^{M} \left(\left| T_1^{(k)} \right| - d - 1 \right) + 2 \sum_{k=1}^{M} \left(\left| T_2^{(k)} \right| - d - 1 \right).$$

Hence, equation (67) simplifies to $\#_{\text{rows}}(A) = \#_{\text{cols}}(A)$, which proves that A is a square matrix.

As for its nonsingularity in the setting of interpolation, suppose that $A\boldsymbol{\alpha} = 0$ for some vector of B-coefficients $\boldsymbol{\alpha}$. Since all knot vectors are open, this immediately implies that all B-coefficients associated to patch vertices are equal to zero. Then, since $\boldsymbol{\alpha}$ satisfies the continuity conditions (because they are homogeneous), the restriction to any edge $C_{k,\ell}$ of the global spline associated to $\boldsymbol{\alpha}$ is well-defined and belongs to the pushforward of the univariate space $S(T_i^{(k)} \cap T_j^{(\ell)}, d)$. The set of Greville abscissas $G_{k,\ell}(T_i^{(k)} \cap T_j^{(\ell)}, d)$ with endpoints removed is unisolvent for the elements of this space vanishing on the boundary. Therefore, all B-coefficients associated to patch edges are equal to zero. Finally, on each patch $\Gamma^{(\ell)}$ the set of bivariate Greville points that do not belong to the boundary of the patch is unisolvent for the elements of the space $S_{h,\mathbf{d}}^{(\ell)}$ vanishing on the boundary of the patch. This proves that $\boldsymbol{\alpha} = 0$, and so A is nonsingular. □

References

[1] J. Cottrell, T. Hughes, Y. Bazilevs, Isogeometric Analysis: Toward Integration of CAD and FEA, John Wiley & Sons, 2009.

[2] G. Farin, J. Hosheck, M.S. Kim, Handbook of Computer Aided Geometric Design, Elsevier, Amsterdam, 2002.

[3] C. de Boor, A Practical Guide to Splines, revised edition, Applied Mathematical Sciences, vol. 27, Springer-Verlag, New York, 2001.

[4] L. Schumaker, Spline Functions: Basic Theory, Cambridge University Press, 2007.

[5] E. Sande, C. Manni, H. Speleers, Explicit error estimates for spline approximation of arbitrary smoothness in isogeometric analysis, Numer. Math. 144 (2020) 889–929.

[6] C. Politis, A.I. Ginnis, P.D. Kaklis, K. Belibassakis, C. Feurer, An isogeometric bem for exterior potential-flow problems in the plane, in: 2009 SIAM/ACM Joint Conference on Geometric and Physical Modeling, 2009, pp. 349–354.

[7] R. Simpson, S. Bordas, J. Trevelyan, T. Rabczuk, A two-dimensional isogeometric boundary element method for elastostatic analysis, Comput. Methods Appl. Mech. Eng. 209–212 (2012) 87–100.

[8] A. Aimi, M. Diligenti, M. Sampoli, A. Sestini, Isogeometric analysis and symmetric Galerkin BEM: a 2D numerical study, Appl. Math. Comput. 272 (2016) 173–186.

[9] G. Beer, B. Marussig, C. Duenser, The Isogeometric Boundary Element Method, Springer, 2020.

[10] Q. Zang, J. Liu, W. Ye, G. Lin, Isogeometric boundary element for analyzing steady-state heat conduction problems under spatially varying conductivity and internal heat source, Comput. Math. Appl. 80 (7) (2020) 1767–1792.

[11] G. Gantner, D. Praetorius, Adaptive BEM for elliptic PDE systems, part II: isogeometric analysis with hierarchical B-splines for weakly-singular integral equations, Comput. Math. Appl. 117 (2022) 74–96.

[12] A. Falini, C. Giannelli, T. Kanduč, M.L. Sampoli, A. Sestini, A collocation IGA-BEM for 3D potential problems on unbounded domains, in: Geometric Challenges in Isogeometric Analysis, Springer, 2022, pp. 31–47.

[13] S. Kirkup, The boundary element method in acoustics: a survey, Appl. Sci. 9 (2019) 1642.

[14] R. Simpson, M. Scott, M. Taus, D. Thomas, H. Lian, Acoustic isogeometric boundary element analysis, Comput. Methods Appl. Mech. Eng. 269 (2014) 265–290.

[15] J. Venas, T. Kvamsdal, Isogeometric boundary element method for acoustic scattering by a submarine, Comput. Methods Appl. Mech. Eng. 359 (2020) 112670.

[16] A. Shaaban, C. Anitescu, E. Atroshchenko, T. Rabczuk, 3D isogeometric boundary element analysis and structural shape optimization for Helmholtz acoustic scattering problems, Comput. Methods Appl. Mech. Eng. 384 (2021) 113950.

[17] A. Falini, T. Kanduč, M. Sampoli, A. Sestini, Cubature rules based on bivariate spline quasi-interpolation for weakly singular integrals, in: G. Fasshauer, M. Neamtu, L. Schumaker (Eds.), Approximation Theory XVI: Nashville 2019, Springer, 2021, pp. 73–86.

[18] A. Aimi, F. Calabrò, M. Diligenti, M. Sampoli, G. Sangalli, A. Sestini, Efficient assembly based on B-spline tailored quadrature rules for the IgA-SGBEM, Comput. Methods Appl. Mech. Eng. 331 (2018) 327–342.

[19] T. Kanduč, Isoparametric singularity extraction technique for 3D potential problems in BEM, Comput. Methods Appl. Mech. Eng. 398 (2022) 115271.

[20] D. Grebenkov, D. Nguyen, Geometrical structure of Laplacian eigenfunctions, SIAM Rev. 55 (4) (2013) 601–667.

[21] J. Venas, T. Jenserud, Exact 3D scattering solutions for spherical symmetric scatterers, J. Sound Vib. 440 (2019) 439–479.

[22] K. Atkinson, The Numerical Solution of Integral Equations of the Second Kind, Cambridge Monographs on Applied and Computational Mathematics, Cambridge University Press, New York, 1997.

[23] Y. Wang, D. Benson, Multi-patch nonsingular isogeometric boundary element analysis in 3D, Comput. Methods Appl. Mech. Eng. 293 (2015) 71–91.

[24] P. Kagan, A. Fischer, P.Z. Bar-Yoseph, Mechanically based models: adaptive refinement for b-spline finite element, Int. J. Numer. Methods Biomed. Eng. 57 (8) (2003) 1145–1175.

[25] J. Cottrell, T. Hughes, A. Reali, Studies of refinement and continuity in isogeometric structural analysis, Comput. Methods Appl. Mech. Eng. 196 (41–44) (2007) 4160–4183.

[26] S.G. Mikhlin, S. Prößdorf, Singular Integral Operators, vol. 68, Springer Science & Business Media, 1987.

[27] M. Taus, G.J. Rodin, T.J. Hughes, Isogeometric analysis of boundary integral equations: high-order collocation methods for the singular and hyper-singular equations, Math. Models Methods Appl. Sci. 26 (08) (2016) 1447–1480.

[28] C. Bracco, C. Giannelli, F. Mazzia, A. Sestini, Bivariate hierarchical Hermite spline quasi-interpolation, BIT Numer. Math. 56 (4) (2016) 1165–1188.

[29] F. Mazzia, A. Sestini, The BS class of Hermite spline quasi-interpolants on nonuniform knot distributions, BIT 49 (3) (2009) 611–628.

[30] F. Calabrò, A. Falini, M. Sampoli, A. Sestini, Efficient quadrature rules based on spline quasi-interpolation for application to IgA-BEMs, J. Comput. Appl. Math. 338 (2018) 153–167.

[31] K. Mørken, Some identities for products and degree raising of splines, Contr. Approx. 7 (1991) 195–208.

[32] A. Falini, C. Giannelli, T. Kanduč, M.L. Sampoli, A. Sestini, An adaptive IgA-BEM with hierarchical B-splines based on quasi-interpolation quadrature schemes, Int. J. Numer. Methods Eng. 117 (10) (2019) 1038–1058.

[33] F. Mazzia, A. Sestini, Quadrature formulas descending from BS Hermite spline quasi-interpolation, J. Comput. Appl. Math. 236 (2012) 4105–4118.

[34] L. Shampine, Vectorized adaptive quadrature in MATLAB, J. Comput. Appl. Math. 211 (2) (2008) 131–140.

[35] M.G. Duffy, Quadrature over a pyramid or cube of integrands with a singularity at a vertex, SIAM J. Numer. Anal. 19 (6) (1982) 1260–1262.

[36] L. af Klinteberg, C. Sorgentone, A. Tornberg, Quadrature error estimates for layer potentials evaluated near curved surfaces in three dimensions, Comput. Math. Appl. 111 (2022) 1–19.

[37] J. Cobb, Tiling the sphere with rational Bézier patches, Technical report UUCS-88-009, Computer Science, University of Utah, 1988.

[38] J. Dölz, H. Harbrecht, S. Kurz, S. Schöps, F. Wolf, A fast isogeometric BEM for the three dimensional Laplace- and Helmholtz problems, Comput. Methods Appl. Mech. Eng. 330 (2018) 83–101.

[39] S.N. Chandler-Wilde, I.G. Graham, S. Langdon, E.A. Spence, Numerical-asymptotic boundary integral methods in high-frequency acoustic scattering, Acta Numer. 21 (2012) 89–305.

[40] J. Bowman, T. Senior, P. Uslenghi, Electromagnetic and Acoustic Scattering, by simple shapes (Revised edition) North-Holland Publishing Company, 1987.